Strong-field tidal distortions of rotating black holes. II. Horizon dynamics from eccentric and inclined orbits

Stephen O'Sullivan and Scott A. Hughes

Strong-field tidal distortions of rotating black holes:
II. Horizon dynamics from eccentric and inclined orbits

Stephen O'Sullivan[1] and Scott A. Hughes[1]

[1]*Department of Physics and MIT Kavli Institute,*
Massachusetts Institute of Technology, Cambridge, MA 02139

In a previous paper, we developed tools for studying the horizon geometry of a Kerr black hole that is tidally distorted by a binary companion using techniques that require large mass ratios but can be applied to any bound orbit and allow for arbitrary black hole spin. We now apply these tools to generic Kerr black hole orbits. This allows us to investigate horizon dynamics: the tidal field perturbing the horizon's geometry varies over a generic orbit, with significant variations for eccentric orbits. Many of the features of the horizon's behavior found previously carry over to the dynamical case in a natural way. In particular, we find significant offsets between the applied tide and the horizon's response. This leads to bulging in the horizon's geometry which can lag or lead the orbit, depending upon the hole's rotation and the orbit's geometry. An interesting and apparently new feature we find are small-amplitude, high-frequency oscillations in the horizon's response. We have not been able to identify a mechanism for producing these oscillations, but find that they appear most clearly when rapidly rotating black holes are distorted by very strong-field orbits.

I. INTRODUCTION

The study of relativistic tidal deformations and their impact on the dynamics of compact binaries has received a great deal of attention in recent years. Much of this recent activity was kicked off by studies of tides in systems containing neutron stars [1–8]. Older work had already demonstrated that tidal coupling was quite important in systems containing black holes, but used language that clouded the role of tides, using instead a dual description of tidal coupling as "radiation down the event horizon" [9–12]. Recent papers focusing on black holes in binaries have examined in detail how tides distort black holes and their near-hole geometry. Most of these papers have focused on non-rotating [5, 13–16] and slowly rotating [17–19] black holes (with Ref. [19] discussing tidal distortions of a broad class of spinning objects).

Our contribution to this body of work has been to develop numerical tools for characterizing tidally distorted black holes which are good for strong-field orbits and arbitrary black hole spins. These tools are based on black hole perturbation theory, and so assume binaries of extreme mass ratio: the mass μ of the small body which is the source of the tide is much less than the mass M of the black hole that is tidally distorted. In Ref. [20] (hereafter "paper I"), we developed tools for characterizing the tidal field that acts on a Kerr black hole. The tools are designed in order to adapt pre-existing codes which have been used to study gravitational wave emission from extreme mass ratio binaries (e.g., [21]). We also developed tools to visualize a tidally distorted black hole by embedding the two-dimensional horizon at each moment in some time slicing in a flat three-dimensional Euclidean space. These embeddings are only good for Kerr spin parameter $a/M \leq \sqrt{3}/2$; for higher spins, the horizon cannot be globally embedded in a Euclidean space even in the absence of a distorting tide [22].

Although the tools we developed in paper I are generic and can be applied to any bound Kerr black hole orbit, we only showed results for tidal distortions arising from circular and equatorial orbits. By focusing on this relatively simple case, we were able to examine some of the key aspects of event horizon physics in a particularly clean limit. For example, paper I examined in some detail the phase offset between the angle at which the horizon is maximally distorted (the location of its "tidal bulge") and the position of the orbit. As has been amply discussed in past literature [23–26], the event horizon acts in many ways like the surface of a gravitating fluid body; a very readable summary discussion of this connection can also be found in Cardoso and Pani [27]. The horizon is deformed by tidal stresses, tending to bulge toward the "moon" which is the source of the tide. The bulging response is, however, not synchronous with the applied tide. For a fluid body, viscosity causes the fluid's response to lag the applied tide. As a consequence, if the moon's orbit is faster than the body's spin, the bulge lags the orbit's position. Conversely, if the orbit is slower than the spin, then the bulge leads the orbit's position.

At least for very slowly varying tidal fields, this picture describes the geometry of the black hole's tidal bulge with respect to the orbit — provided we swap "lead" and "lag." Tides from a moon which orbits faster than the hole's spin raise a bulge which *leads* the orbit's position; tides from a moon which orbits more slowly *lag* the orbit's position. The swap of "lead" and "lag" as compared to the fluid star is due to the *teleological* nature of the event horizon: how the horizon depends at some moment in a given time slicing depends upon the stresses that it will feel in the future. Though this counterintuitive behavior might seem to violate causality, it is a simple consequence of how the horizon is defined: whether an event is inside or outside the horizon depends on that event's future. See paper I and references therein (as well as the references

cited above) for much more detailed discussion of the horizon's teleological nature and its consequences.

Although circular and equatorial orbits were useful for testing our tidal distortion toolkit, this limit does not show the full range of horizon dynamics that can be expected from tidal interactions. Indeed, the horizon's distortion is stationary in this case, showing no variation at all in a frame that co-rotates with the orbit. The purpose of this paper is to go beyond this limit and to explore how the horizon responds to generic — inclined and eccentric — orbits. Generic orbits and the tides they produce are dynamical even when examined in a frame that corotates at the orbit's axial frequency. Eccentricity is particularly important: at leading order the tidal field varies as $1/r^3$, so as the orbit's radius varies from $r_{\max}$ to $r_{\min}$, the tidal field varies by a factor $r_{\max}^3/r_{\min}^3$. If the large black hole spins, even constant radius inclined orbits show horizon dynamics, since the on-horizon tidal field varies as the orbit moves in the non-spherical black hole spacetime.

The remainder of this paper is organized as follows. We begin in Sec. II with a summary of the formalism that we developed in paper I. Section II A introduces the notation and conventions that we use, and carefully defines several quantities that are critical to our analysis, such as the Newman-Penrose basis legs, the tidal field Ψ_0, and the horizon's shear σ. This section also briefly describes the techniques we use to compute these quantities; further details are given in paper I. Appendix A supplements this material, demonstrating that the complex fields we use for various quantities needed to describe the horizon's distortion are equivalent to certain 2nd-rank tensors defined on the horizon which other authors have used (notably Ref. [16], hereafter VPM11). Section II B summarizes how these quantities are used to understand the distorted horizon's geometry.

We show our results in Secs. III, IV, V, and VI. Much of the horizon's dynamics turns out to be closely correlated to the dynamics of the applied tidal field, so we begin in Sec. III by examining this tide in some detail. We show that the vast majority of the tide's behavior can be understood as a simple consequence of the orbital dynamics. There are, however, subtle features related to a position-dependent phase and a mode-dependent amplitude correction that must be explained with some care. We turn to the horizon's response proper in Sec. IV, carefully examining the Schwarzschild limit, $a = 0$. This limit is spherically symmetric, so the horizon distortions must exhibit certain symmetries as an orbit is inclined from equatorial to some arbitrary inclination $\theta_{\rm inc}$. We demonstrate that this is the case. This is not a surprise, since the black hole perturbation theory code on which our analysis is based has previously been shown to handle this limit correctly [11, 21]. It is reassuring to see that the modifications we made to analyze distorted horizons have not broken this behavior.

In Sec. V, we next compare certain important aspects of the applied tidal field Ψ_0 to the horizon shear σ that arises from this field. We first (Sec. V A) look at the rel-

ative phase of the tide and the shear, an analysis quite similar to one that we undertook in paper I. We focus for simplicity on equatorial orbits. In the Schwarzschild limit, the tide and the shear are very similar. Much of the difference between the two quantities is due to a simple temporal offset of $\kappa^{-1} = 4M$ (where κ is the event horizon's surface gravity). This offset can be understood by examining the equation relating the ride to the shear in the frequency domain. The difference becomes much less simple as the black hole's spin is increased.

It's worth noting that some of the physics associated with the offset between the orbiting body and the horizon's distortion that we discussed above is reproduced in the tide-shear analysis. In particular, we find that the shear response leads the applied tidal field for $a = 0$, but lags it for large black hole spin — just as the horizon bulge always leads the orbit in Schwarzschild, but lags the orbit for rapidly spinning Kerr. Because the tide and the shear are evaluated at the same coordinate radius, many ambiguities associated with comparing the position of the horizon's bulge with the position of the orbit disappear. This helps to put notions of which quantities "lead" and "lag" on a firm footing.

In the course of this analysis, we have found an interesting oscillatory feature in the horizon's response which is most apparent for strong-field orbits of rapidly rotating black holes. Examining the response of a black hole with spin $a = 0.9999M$ to the tidal field of a strong-field eccentric orbit, we see a very strong response near periapse with properties that closely correlate to the near-periapsis orbital dynamics. This is followed by about seven cycles of low-amplitude, high-frequency oscillations in the horizon's response. We do not see corresponding oscillations in the tide.

Although we can estimate the frequency of these oscillations fairly well, we have not been able to connect them to any of the frequencies that describe this orbit or this black hole. The rate at which the oscillations decay also does not appear to correlate with any timescale that we can imagine would lead to such behavior. Having not succeeded in coming up with a compelling explanation for this phenomenon, for now we simply present it as an empirical finding of our analysis, hoping that future work may offer some physical understanding.

We conclude by examining the dynamics of horizon embeddings in Sec. VI. For several representative cases, we show a sequence of still images taken from an animation that combines the behavior of the small body's orbit with the dynamics of the horizon embedding. Those animations can be found at the URL listed in Ref. [28]. Although we have endeavored to describe the dynamics as clearly as possible using these stills, some of these results are particularly clear when examined with the animations. We first consider orbits that are circular but inclined in Sec. VI A, examining in detail orbits of a Schwarzschild black hole and of a Kerr hole with $a = 0.6M$. The Schwarzschild results confirm our expectations from Sec. IV about how the horizon should

behave in this spherically symmetric example. The non-spherical Kerr results show more interesting shape dynamics. We then consider eccentric orbits in Sec. VI B. As expected, the horizon's distortion varies considerably as an orbit moves from $r_{\rm max}$ to $r_{\rm min}$ and back. We examine in some detail two highly eccentric ($e = 0.7$) orbits: one that is equatorial, and one inclined at $\theta_{\rm inc} = 30°$. The generic case combines features that we see from the inclined circular and the eccentric equatorial limits.

II.   SUMMARY OF FORMALISM

A.   Tools, notation, and conventions

All of our calculations are performed in the spacetime of a Kerr black hole with mass M and spin angular momentum J. Throughout this analysis, we work in ingoing coordinates (v, r, θ, ψ) which are well behaved on the black hole's event horizon. In these coordinates, the spacetime's line element is given by

$$ds^2 = -\left(1 - \frac{2Mr}{\Sigma}\right) dv^2 + 2dv\, dr - 2a\sin^2\theta\, dr\, d\psi$$
$$- \frac{4Mar\sin^2\theta}{\Sigma} dv\, d\psi + \Sigma\, d\theta^2$$
$$+ \frac{(r^2 + a^2)^2 - a^2\Delta\sin^2\theta}{\Sigma} d\psi^2 , \qquad (2.1)$$

with $a = J/M$. (Here and throughout the paper, we use units in which $G = 1 = c$.) Equation (2.1) introduces the functions $\Delta = r^2 - 2Mr + a^2$ and $\Sigma = r^2 + a^2\cos^2\theta$. The event horizon is at coordinate radius $r = r_+ = M + \sqrt{M^2 - a^2}$, the larger root of Δ. Although not needed here, for completeness we note that ingoing coordinates are simply related to the more commonly used Boyer-Lindquist coordinates (t, r, θ, ϕ): the coordinates r and θ are identical, and the ingoing time v and angle ψ are related to Boyer-Lindquist time t and angle ϕ via

$$dv = dt + \frac{r^2 + a^2}{\Delta} dr , \qquad (2.2)$$
$$d\psi = d\phi + \frac{a}{\Delta} dr . \qquad (2.3)$$

The tidal field which distorts the black hole's horizon arises from a small body on a bound Kerr geodesic; detailed discussion of these orbits, with an emphasis on the properties relevant to this analysis, is given in Refs. [29, 30]. Such geodesics are parameterized by three conserved integrals: the orbital energy E, related to the spacetime's timelike Killing vector; the axial angular momentum L_z, related to the spacetime's axial Killing vector; and the Carter constant Q, related to the Kerr spacetime's Killing tensor. Once E, L_z, and Q have been selected, the orbit's motion is determined up to initial conditions. A particularly important feature of bound Kerr orbits is that they are triperiodic [29]. Each orbit

has a frequency Ω_r which describes radial oscillations, a frequency Ω_θ which describes polar oscillations, and a frequency Ω_ϕ which describes rotations about the black hole's spin axis. Once E, L_z, and Q are known, it is not too difficult to compute Ω_r, Ω_θ, and Ω_ϕ [29, 30].

We remap the motion in r and θ to the parameters p (semi-latus rectum), e (eccentricity), and $\theta_{\rm m}$, defined by

$$r = \frac{p}{1 + e\cos\chi_r} , \qquad (2.4)$$
$$\cos\theta = \cos\theta_{\rm m}\cos(\chi_\theta + \chi_{\theta,0}) . \qquad (2.5)$$

The orbit's radius r thus oscillates between periapsis $r_{\rm min} = p/(1 + e)$ and apoapsis $r_{\rm max} = p/(1 - e)$; the polar angle θ oscillates between $\theta_{\rm min} = \theta_{\rm m}$ and $\theta_{\rm max} = 180° - \theta_{\rm m}$.

With the parameterization (2.4) and (2.5), the geodesic equations for the coordinates r and θ become equations for the angles χ_r and χ_θ. Note that we could include an offset phase $\chi_{r,0}$ in Eq. (2.4). We have set $\chi_{r,0} = 0$, which is equivalent to setting the origin of our time coordinate to the moment that the orbit passes through periapsis. References [29, 30] give easy-to-use expressions relating the (E, L_z, Q) and $(p, e, \theta_{\rm m})$ parameterizations. For much of our analysis, we use the angle $\theta_{\rm inc}$ introduced in Ref. [21] in place of $\theta_{\rm m}$:

$$\theta_{\rm inc} = 90° - {\rm sgn}(L_z)\theta_{\rm m} . \qquad (2.6)$$

This angle varies smoothly from 0 to 180° as the orbit varies from prograde equatorial ($\theta_{\rm m} = 90°$, $L_z > 0$) to retrograde equatorial ($\theta_{\rm m} = 90°$, $L_z < 0$).

The tidal field is quantified by the complex scalar field[1] Ψ_0, which is built from the Weyl curvature tensor:

$$\Psi_0 = -C_{\mu\alpha\nu\beta} l^\mu m^\alpha l^\nu m^\beta . \qquad (2.7)$$

The vectors used here are the Newman-Penrose null legs in the Hawking-Hartle representation [23]:

$$l^\mu \doteq \left[1, \frac{\Delta}{2\varpi^2}, 0, \frac{a}{\varpi^2}\right] , \qquad (2.8)$$
$$n^\mu \doteq \frac{1}{\Sigma}\left[-a^2\sin^2\theta/2, -\varpi^2 + \frac{a^2\Delta\sin^2\theta}{4\varpi^2}, 0,\right.$$
$$\left. -a + \frac{a^3\sin^2\theta}{2\varpi^2}\right] , \qquad (2.9)$$
$$m^\mu \doteq \frac{1}{\sqrt{2}(r + ia\cos\theta)}\left[0, -\frac{ia\Delta\sin\theta}{\varpi^2}, 1,\right.$$
$$\left. i\csc\theta - \frac{ia^2\sin\theta}{\varpi^2}\right] . \qquad (2.10)$$

The symbol $\doteq$ means "the components of the quantity on the left-hand side are represented by the array on the

_____

[1] In this paper, we use capital Ψ rather than the more commonly used lowercase ψ to denote the Weyl curvature scalars in order to avoid confusion with the ingoing axial coordinate.

right-hand side in ingoing Kerr coordinates." For brevity, we have introduced $\varpi^2 = r^2 + a^2$. These legs satisfy

$$l^\mu n_\mu = -1 , \qquad m^\mu \bar{m}_\mu = 1 , \qquad (2.11)$$

with overbar denoting complex conjugate; all other inner products between legs vanish.

Following VPM11, the Weyl curvature on the horizon is completely described by a two-dimensional trace-free symmetric tensor C_{AB}, where capital Roman indices denote components associated with coordinates on the horizon. Such a tensor has only two independent components, which we can describe as "tidal polarizations," and denote C_+ and $C_\times$. These polarizations are simply related to the curvature scalar Ψ_0 on the horizon:

$$\Psi_0(r_+) = -(C_+ + iC_\times) . \qquad (2.12)$$

See App. A for further details and a proof of Eq. (2.12). We use the polarizations $C_{+,\times}$ in much of our presentation of results, especially in Sec. V.

The tidal field can be decomposed into harmonics of the three fundamental Kerr frequencies, allowing us to write its value at $r = r_+$ as

$$\Psi_0(v,\theta,\psi) = \frac{1}{16M^2 r_+^2} \sum_{lmkn} W^{\mathrm{H}}_{lmkn} S^+_{lmkn}(\theta) e^{i\Phi_{mkn}(v,\psi)} . \qquad (2.13)$$

The function

$$S^+_{lmkn}(\theta) = {}_{+2}S_{lm}(\theta; a\omega_{mkn}) \qquad (2.14)$$

is a spheroidal harmonic of spin-weight $+2$; detailed discussion of this function and how it is computed can be found in Ref. [11]. The frequency ω_{mkn} is a harmonic of the orbital frequencies,

$$\omega_{mkn} = m\Omega_\phi + k\Omega_\theta + n\Omega_r . \qquad (2.15)$$

The product $a\omega_{mkn}$ sets the "oblateness" associated with $S^+_{lmkn}(\theta)$. We describe the phase $\Phi_{mkn}(v,\psi)$ in more detail below.

The amplitude W^{H}_{lmkn} can be found by solving the Teukolsky equation [9]. In practice, we compute the field Ψ_4, a different projection of the Weyl curvature. In the limits $r \to r_+$ and $r \to \infty$, the fields Ψ_4 and Ψ_0 can be related to one another without too much trouble [10]. As $r \to r_+$, Ψ_4 takes the form

$$\Psi_4 = \frac{\Delta^2}{(r - ia\cos\theta)^4} \sum_{lmkn} Z^{\mathrm{H}}_{lmkn} S^-_{lmkn}(\theta) e^{i\Phi_{mkn}(v,\psi)} . \qquad (2.16)$$

Detailed discussion of how to compute the amplitude Z^{H}_{lmkn} using the Teukolsky equation is given in Ref. [21]. The function

$$S^-_{lmkn}(\theta) = {}_{-2}S_{lm}(\theta; a\omega_{mkn}) \qquad (2.17)$$

is a spheroidal harmonic of spin-weight -2; see [11] for detailed discussion.

The Starobinsky-Churilov identities [31] connect the amplitudes of these two curvature scalars:

$$W^{\mathrm{H}}_{lmkn} = \beta_{lmkn} Z^{\mathrm{H}}_{lmkn} , \qquad (2.18)$$

where

$$\beta_{lmkn} = \frac{64(2Mr_+)^4 p_{mkn}(p_{mkn}^2 + \kappa^2)(p_{mkn} + 2i\kappa)}{c_{lmkn}} , \qquad (2.19)$$

$$\begin{aligned} |c_{lmkn}|^2 = & \{[(\lambda+2)^2 + 4ma\omega_{mkn} - 4a^2\omega_{mkn}^2] \\ & \times (\lambda^2 + 36ma\omega_{mkn} - 36a^2\omega_{mkn}^2) \\ & + (2\lambda+3)(96a^2\omega_{mkn}^2 - 48ma\omega_{mkn})\} \\ & + 144\omega_{mkn}^2(M^2 - a^2) , \qquad (2.20) \end{aligned}$$

$$\mathrm{Im}\, c_{lmkn} = (-1)^{l+k+m} 12M\omega_{mkn} , \qquad (2.21)$$

$$\mathrm{Re}\, c_{lmkn} = +\sqrt{|c_{lmkn}|^2 - 144M^2\omega_{mkn}^2} . \qquad (2.22)$$

In these equations,

$$p_{mkn} = \omega_{mkn} - m\Omega_{\mathrm{H}} , \qquad (2.23)$$

with $\Omega_{\mathrm{H}} = a/2Mr_+$, the angular frequency associated with the Kerr event horizon. The real number λ is related to the eigenvalue of the spheroidal harmonic:

$$\lambda = \mathcal{E} - 2am\omega_{mkn} + a^2\omega_{mkn}^2 - s(s+1) , \qquad (2.24)$$

where $s = -2$, and $\mathcal{E}$ is the eigenvalue[2] associated with the $s = -2$ spheroidal harmonic. In the limit $a = 0$, $\mathcal{E} = l(l+1)$. Note that the imaginary part of c_{lmkn} is positive for "polar" modes ($l+k+m$ even), and is negative for "axial" modes ($l + k + m$ odd). This sign is given incorrectly in many papers in the literature, including the first one in which the constant is computed [10]. We discuss this error briefly in an erratum which was recently published for Ref. [20]; further discussion will be given in a forthcoming paper by Flanagan and Hinderer [38].

Other important quantities appearing in these equations are the black hole's surface gravity,

$$\kappa = \frac{\sqrt{M^2 - a^2}}{2Mr_+} , \qquad (2.25)$$

and the phase

$$\Phi_{mkn}(v,\psi) = m[\psi - K(a)] - (m\Omega_\phi + k\Omega_\theta + n\Omega_r)v , \qquad (2.26)$$

where

$$\begin{aligned} K(a) = & \frac{a}{2M(Mr_+ - a^2)}\bigg\{a^2 - Mr_+ \\ & + 2M^2\mathrm{arctanh}\left(\sqrt{1 - a^2/M^2}\right) \\ & + M\sqrt{M^2 - a^2}\ln\left[\frac{a^2}{4(M^2 - a^2)}\right]\bigg\} . \quad (2.27) \end{aligned}$$

———

[2] Multiple conventions for this eigenvalue can be found in the literature. Another common one puts $\lambda = A - 2am\omega_{mkn} + a^2\omega_{mkn}^2$; they are related by $A = \mathcal{E} - s(s+1)$.

In Eqs. (2.13) and (2.16), the sum over l goes from 2 to ∞; the sum over m from $-l$ to l; and the sums over k and n from $-\infty$ to ∞. We abbreviate this set of indices $\Lambda \equiv \{l, m, k, n\}$. With this, Eq. (2.13) becomes

$$\Psi_0(v, \theta, \psi) = \frac{1}{16M^2 r_+^2} \sum_\Lambda W_\Lambda^{\mathrm{H}} S_\Lambda^+(\theta) e^{i\Phi_\Lambda(v,\psi)}$$

$$\equiv \sum_\Lambda \Psi_{0,\Lambda} S_\Lambda^+(\theta) e^{i\Phi_\Lambda(v,\psi)} . \qquad (2.28)$$

We have introduced

$$\Psi_{0,\Lambda} = \frac{W_\Lambda^{\mathrm{H}}}{16M^2 r_+^2}$$

$$= \frac{64M^2 r_+^2 p_\Lambda (p_\Lambda^2 + \kappa^2)(p_\Lambda + 2i\kappa) Z_\Lambda^{\mathrm{H}}}{c_\Lambda} . (2.29)$$

Note that the phase $\Phi_\Lambda \equiv \Phi_{mkn}$ and wavenumber $p_\Lambda \equiv p_{mkn}$ don't actually depend on the index l. Using Λ as a label for these quantities is thus somewhat redundant, though this redundancy is harmless.

B. The geometry of a distorted event horizon

1. The shear to the horizon's generators

The first tool we need to understand how the tidal field affects the horizon's geometry is the shear σ of the horizon's generators. It is given by

$$\sigma = m^\mu m^\nu \nabla_\mu l_\nu , \qquad (2.30)$$

evaluated at $r = r_+$. (Note that, for an unperturbed black hole, l^μ is tangent to the generators at $r = r_+$.) Just as the complex Weyl scalar Ψ_0 can be written using polarizations $C_{+,\times}$ of the on-horizon Weyl tensor, the complex shear can be written in terms of polarizations $\sigma_{+,\times}$ of an on-horizon shear tensor:

$$\sigma = \sigma_+ + i\sigma_\times . \qquad (2.31)$$

See App. A for further details and a proof of Eq. (2.31). We will use $\sigma_{+,\times}$ in much of our discussion of results, especially in Sec. V.

With the tetrad and gauge that we use, the perturbed shear is governed by the equation [25]

$$(D - \kappa)\sigma = \Psi_0 , \qquad (2.32)$$

where the derivative operator $D \equiv l^\mu \partial_\mu$. Let us expand σ as we expanded Ψ_0:

$$\sigma(v, \theta, \psi) = \sum_\Lambda \sigma_\Lambda S_\Lambda^+(\theta) e^{i\Phi_\Lambda(v,\psi)} . \qquad (2.33)$$

Using the fact that $D \to \partial_v + \Omega_{\mathrm{H}} \partial_\psi$ on the horizon, we find that Eq. (2.32) is satisfied if

$$\sigma_\Lambda = 64M^2 r_+^2 c_\Lambda^{-1} p_\Lambda (p_\Lambda + i\kappa)(ip_\Lambda - 2\kappa) Z_\Lambda^{\mathrm{H}} .$$

As was extensively discussed in paper I, there is a phase offset between the shear and the applied tidal field. The phase offset for each mode is simple to calculate:

$$\frac{\sigma_\Lambda}{\Psi_{0,\Lambda}} = \frac{i}{p_\Lambda - i\kappa} = \frac{\exp\left[-i \arctan(p_\Lambda/\kappa)\right]}{\sqrt{p_\Lambda^2 + \kappa^2}} . \qquad (2.34)$$

In other words, for each mode, the shear leads the tide by an angle given by the mode's wavenumber p_Λ times the inverse surface gravity κ^{-1}. For circular and equatorial orbits, $p_\Lambda \to m(\Omega_\phi - \Omega_{\mathrm{H}})$, so each mode experiences the same phase shift, modulo m. For these orbits, we find a simple, constant offset between the tidal field and the resulting shear. More complicated behavior results for generic orbits, since many modes, each with different phase shifts, contribute to Ψ_0 and σ.

Although we do all of our calculations in this paper in the frequency domain, it is also useful to examine Eq. (2.32) in a "time-like" domain. As mentioned above, the Newman-Penrose leg l^μ is tangent to the unperturbed horizon generators at $r = r_+$. We may therefore write $D \equiv d/d\lambda$ on the horizon, where λ is affine parameter along the generator. In this representation, λ is effectively a time measure, albeit a somewhat unusual time, measured by a clock that ticks at a uniform rate as it follows a specific horizon generator.

With this in mind, following Ref. [26] Sec. VI C 6, let us find the Green's function $G(\lambda, \lambda')$ for Eq. (2.32):

$$(D - \kappa)G(\lambda, \lambda') = \delta(\lambda - \lambda') . \qquad (2.35)$$

This equation has the solution

$$G(\lambda, \lambda') = -e^{\kappa(\lambda - \lambda')}\Theta(\lambda' - \lambda) , \qquad (2.36)$$

where the step function

$$\Theta(x) = 1 \qquad x > 0$$
$$= 0 \qquad x < 0 . \qquad (2.37)$$

The shear along the generator is then

$$\sigma(\lambda) = -\int_\lambda^\infty e^{\kappa(\lambda - \lambda')}\Psi_0(\lambda')d\lambda' , \qquad (2.38)$$

or, using Eqs. (2.12) and (2.31),

$$\sigma_{+,\times}(\lambda) = \int_\lambda^\infty e^{\kappa(\lambda - \lambda')}C_{+,\times}(\lambda')d\lambda' . \qquad (2.39)$$

Notice that the behavior at λ depends on the tides *to the future* of λ — a manifestation of the horizon's teleological nature. What we see is that the shear at λ on a particular generator depends on the tide integrated over an interval from λ to $\lambda + $ (a few) $\times \kappa^{-1}$.

2. The curvature of the distorted horizon

The tidal field Ψ_0 on the horizon also tells us the scalar Ricci curvature of the black hole, R_{H}. This is discussed

in great detail in paper I. Briefly, the scalar curvature of the hole's event horizon is given by

$$R_{\text{H}} = R_{\text{H}}^{(0)} + R_{\text{H}}^{(1)} \; , \qquad (2.40)$$

where

$$R_{\text{H}}^{(0)} = \frac{2}{r_+^2} \frac{(1 + a^2/r_+^2)(1 - 3a^2 \cos^2\theta/r_+^2)}{(1 + a^2 \cos^2\theta/r_+^2)^3} \qquad (2.41)$$

describes an undistorted Kerr black hole, and

$$R_{\text{H}}^{(1)} = -4\text{Im} \sum_\Lambda \frac{\bar{\eth}\bar{\eth}\Psi_{0,\Lambda}}{p_\Lambda(ip_\Lambda + \kappa)} \qquad (2.42)$$

is the perturbation to R_{H} arising from the tidal field Ψ_0. The operator $\bar{\eth}$ lowers the spin weight of the angular basis functions. As discussed in Sec. IIC of paper I, it is quite simple to evaluate $\bar{\eth}\bar{\eth}\Psi_{0,\Lambda}$ with the spectral expansion for the spin-weighted spheroidal harmonics that we use. See paper I for detailed discussion.

To visualize the curvature of a distorted horizon, we embed the horizon in a global Euclidean 3-space. This means finding the function

$$r_{\text{E}}(\theta,\psi) = r_{\text{E}}^{(0)}(\theta) + r_{\text{E}}^{(1)}(\theta,\psi) \qquad (2.43)$$

that defines a surface with the same Ricci scalar curvature as the distorted horizon. This works well for spins $a/M < \sqrt{3}/2$; for higher spins, global Euclidean embeddings do not exist even for the undistorted event horizon [22]. As such, we confine our embedding visualizations in this paper to the range $0 \le a/M < \sqrt{3}/2$. Work in progress indicates that an elegant way to lift this restriction will to be embed the horizon's distorted geometry in the globally hyperbolic space H^3 [32].

Confining our discussion to Euclidean 3-space, a simple analytic solution exists for the undistorted hole's embedding radius $r_{\text{E}}^{(0)}(\theta)$ [22]. To find the perturbation $r_{\text{E}}^{(1)}(\theta,\psi)$, we expand in spherical harmonics, writing

$$r_{\text{E}}^{(1)}(\theta,\psi) = r_+ \sum_{\ell m} \varepsilon_{\ell m} Y_{\ell m}(\theta,\psi) \; . \qquad (2.44)$$

Given this form, it is a straightforward (although rather lengthy) exercise to construct the scalar curvature $R_{\text{E}}^{(1)}$ associated with $r_{\text{E}}^{(1)}$; details are given in Appendix B of paper I. By enforcing $R_{\text{E}}^{(1)} = R_{\text{H}}^{(1)}$, we read off the embedding coefficients $\varepsilon_{\ell m}$. Full details of the algorithm for doing this are given in Appendix B of paper I.

III. BEHAVIOR OF THE TIDAL FIELD

Before examining how the horizon responds to dynamical tides, we first look at some examples of tides from geodesic orbits. As we will see in later sections, the shear polarizations $\sigma_{+,\times}$ largely follow the behavior of the driving tides $C_{+,\times}$. There are, however, some features of the shear that are unique. It is thus useful to examine the tide in detail to set a baseline for comparing the two functions' behaviors.

A. Circular inclined orbits

The simplest behavior is seen for circular orbits of Schwarzschild black holes, for which $\Omega_\theta = \Omega_\phi$. These orbits do not precess, instead maintaining a fixed orientation for all time. Figure 1 shows[3] a typical example of the behavior we see in this case. The four panels of this figure all illustrate the tidal field arising from an orbit with $a = 0$, $p = 10M$, $\theta_{\text{inc}} = 60°$. The orbit is oriented so that $\theta = 30°$ at $\psi = 0°$. It crosses the equator at $\psi = 90°$, continues to $\theta = 150°$ at $\psi = 180°$, crosses the equator again at $\psi = 270°$ and returns to $\theta = 30°$ at $\psi = 360°$.

Although simple, the tidal field shown in Fig. 1 demonstrates certain important features which will recur in more complicated examples. Perhaps most significantly, note the strong modulation of the tide's amplitude with azimuthal position ψ. The panels on the left show the tide evaluated at $\psi = 0°$, where the tide is near its maximum; those on the right show it at $\psi = 90°$, near its minimum. The amplitude varies sinusoidally with ψ between these extremes.

The two upper panels show the tidal field including modes up to $l = 9$; the two lower panels only include quadrupole modes ($l = 2$, $m + k = \pm 2$). The quadrupolar tidal field is a pure sinusoid, oscillating twice per orbit. Additional modes complicate this structure, adding features which oscillate at both lower frequency ($m = 1$ modes) and higher frequency.

Consider next the tide arising from circular orbits of Kerr black holes. Two examples are shown in the left-hand panels of Fig. 2. The top example is for spin $a = 0.3M$, and the bottom is for $a = 0.85M$; both examples use $p = 10M$, $\theta_{\text{inc}} = 60°$ and include modes up to $l = 9$. Thanks to frame dragging, the orbit's orientation is not fixed in these cases. The orbit instead precesses about the black hole's spin axis, modulating the tide. This precession causes a modulation of the fields $C_{+,\times}$; they oscillate between bounds similar to those seen in Fig. 1 at $\psi = 0°$ and $\psi = 90°$. This precession is substantially faster at $a = 0.85M$ than at $a = 0.3M$, leading to the more rapid modulation seen in the bottom figure than in the top.

More interestingly, the amplitude is roughly an order of magnitude smaller for $a = 0.3M$ than for $a = 0.85M$. The reason for this can be understood by examining Eq.

---

[3] We use a mass ratio $\mu/M = 1/30$ for all figures which show quantities computed in black hole perturbation theory (such as C_+, σ_+, or the embedding surfaces). This fairly large mass ratio is only used so that the effects we compute are clearly visible in these figures. Since we use linear perturbation theory, one can easily extrapolate to other mass ratios. We also scale these quantities by $r_{\text{min}}^3/M^3 = p^3/[M(1+e)]^3$, accounting for the $1/r^3$ leading-order scaling associated with tides. This makes it easier to compare tidal distortions for different orbits, ensuring that the maximum distortion is roughly the same in all cases we present.
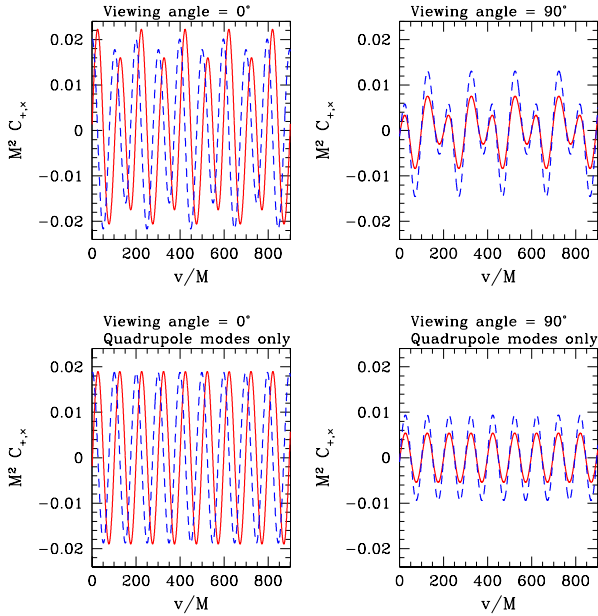
FIG. 1: Examples of the on-horizon tidal field C for circular orbits around a Schwarzschild black hole. The four plots shown here are for an orbit with $p = 10M$ and with inclination angle $\theta_{\rm inc} = 60°$. The solid (red) line shows the polarization C_+; the dashed (blue) line shows $C_\times$. The top two panels illustrate how this field varies with ingoing time v at azimuth angle $\psi = 0°$ and $\psi = 90°$; the bottom two figures show the same data, but including only quadrupolar modes (i.e., modes for which $l = 2$ and $m + k = \pm 2$). These plots illustrate the importance of modes beyond the quadrupole, as well as the strong functional dependence of the tide on the position at which it is measured.

(2.29): each mode of the tidal field is proportional to the wavenumber $p_\Lambda = \omega_\Lambda - m\Omega_{\rm H}$. For $a = 0.3M$, Ω_θ and Ω_ϕ are roughly a factor of two from $\Omega_{\rm H}$ ($M\Omega_\theta = 0.0312$, $M\Omega_\phi = 0.0317$, $M\Omega_{\rm H} = 0.0768$). By contrast, these frequencies are quite different for $a = 0.85M$ ($M\Omega_\theta = 0.0303$, $M\Omega_\phi = 0.0318$, $M\Omega_{\rm H} = 0.2784$). The wavenumber is substantially smaller in the case $a = 0.3M$ for the most important modes of the tide, and the resulting field is of much smaller amplitude. This dependence of tide on p_Λ causes a strong variation of its amplitude as a function of a. The right-hand panel of Fig. 2 shows how, holding the orbit geometry fixed, the amplitude of C_+ varies with a. The effect is quite significant, with the field being a factor ~ 70 larger for nearly maximal Kerr holes than it is for very slow rotation. Although differing in detailed behavior, similar variation of the tide with a is found for other orbits. For example, for strong-field orbits with $(p, e, \theta_{\rm inc})$ fixed, the we typically find a minimal tide at $a/M \sim 0.1 - 0.3$.

B. Eccentric equatorial orbits

Let us now examine tides from eccentric orbits in the black hole's equatorial plane. We again begin with Schwarzschild black holes, and examine the tidal field C_+ for an orbit with $p = 8M$, $e = 0.5$. The left-hand panels of Fig. 3 show the behavior of C_+ close to the moment that the orbit passes through periapsis. We examine this field in the hole's equatorial plane, $\theta = 90°$, and at four evenly spaced axial angles, $\psi = 0°$, $90°$, $180°$, and $270°$. Note that the cross polarization $C_\times$ vanishes for all equatorial orbits, so we do not show it in any of our figures. (Away from the equatorial plane, $C_\times$ is non zero, but is qualitatively quite similar to C_+.) The right-hand panel of Fig. 3 shows the orbit's radius as a function of ingoing time near periapse passage.

The behavior of C_+ at $\psi = 0°$ can be regarded as a prototype for the tidal field from eccentric orbits: there is a large spike at roughly the same time as periapsis, with smaller scale oscillations before and after. These dynamics in C_+ occur when the small body is closest to the event horizon. To quantify this, we have marked with large dots the moments at which the orbital radius is $r = 10^{1/3}r_{\rm min}$ ($v \simeq 295M$ and $v \simeq 475M$). Since at leading order the tide scales as $1/r^3$, we expect that the tide will be about an order of magnitude smaller than its peak at these moments. Comparing the left-hand panels, we see that C_+ in all cases is at least a factor of ten smaller than its peak value at these times.

The remaining three left-hand panels show how the tide is modulated by the azimuthal angle. In all cases, we see three oscillations, but the relative amplitude of these oscillations varies significantly with the value of ψ at which the field is measured: the middle oscillation is "large" and the other two small for the prototypical form we see at $\psi = 0°$, but all three wiggles are of nearly equal amplitude at $\psi = 180°$. As we saw in the circular case (cf. Fig. 1), the position at which the field is measured significantly affects the tide.

Figure 4 examines the tide for eccentric equatorial Kerr black hole orbits. We show C_+ for orbits with $p = 8M$, $e = 0.5$ about black holes with spins $a = 0.3M$, $a = 0.6M$, and $a = 0.9M$, as well as an orbit with $p = 3.5M$, $e = 0.7$ about a black hole with spin $a = 0.9M$. Two of the examples ($p = 8M$, $e = 0.5$ for $a = 0.6M$ and $a = 0.9M$) are similar to the prototype eccentric tide we examined for Schwarzschild (the $\psi = 0°$ case of Fig. 3): a large spike near periapsis, with smaller scale oscillations before and after. The only notably new feature we see in these examples is the rather different amplitude of C_+ as compared to the Schwarzschild case, and as compared to each other. This is explained similarly to how we explained the varying tidal amplitudes of circular Kerr orbits (cf. Fig. 2 and associated discussion): the amplitude of each mode Λ is proportional to $p_\Lambda = \omega_\Lambda - m\Omega_{\rm H}$. Modes can be significantly suppressed when the orbit frequencies are close to $\Omega_{\rm H}$.

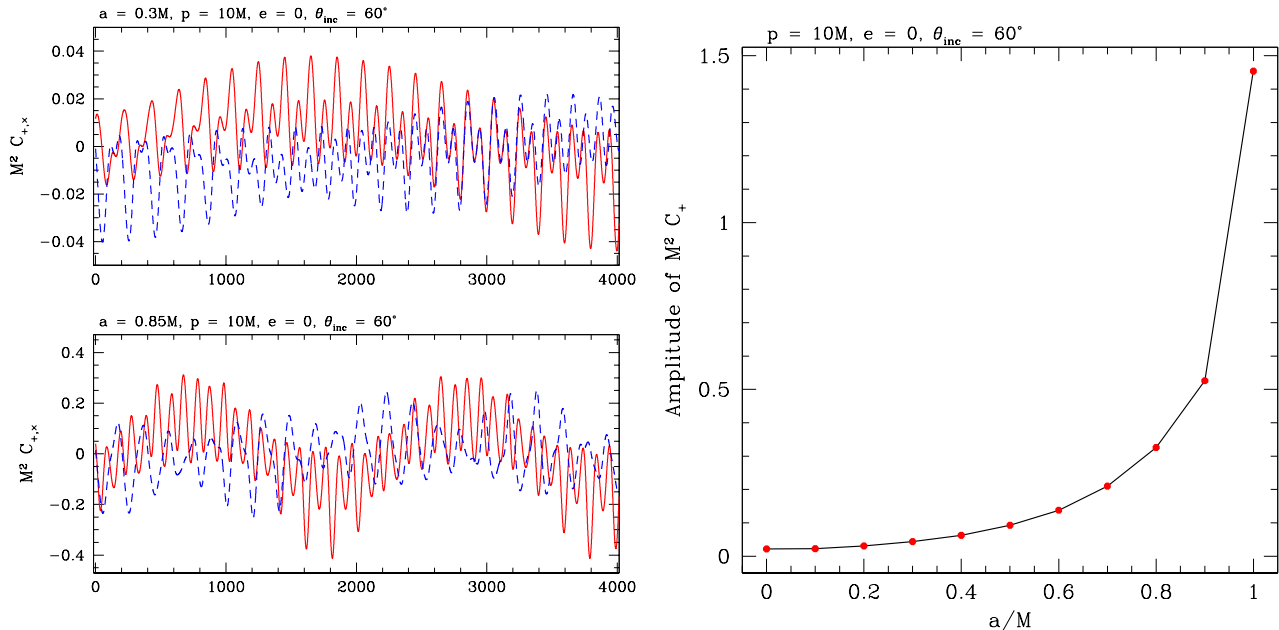The cases $a = 0.3M$, $p = 8M$, $e = 0.5$ (top-left panel

FIG. 2: Examples of the on-horizon tidal polarizations $C_{+,\times}$ for circular orbits around Kerr black holes (left panels), and the amplitude as a function of black hole spin (right panel). All data are for orbits with $p = 10M$, $\theta_{\rm inc} = 60°$. The top plot on the left is for a black hole with spin $a = 0.3M$; bottom is for a hole with spin $a = 0.85M$. Notice that the amplitude is significantly smaller for $a = 0.3M$, and that the modulation is significantly slower. The difference in modulation is simply explained: frame dragging is substantially stronger at $a = 0.85M$, so the orbit precesses much more rapidly. The amplitude effect is more subtle. Each mode Λ of the on-horizon tidal field is proportional to $p_\Lambda \equiv \omega_\Lambda - m\Omega_{\rm H}$. At $a = 0.3M$, both Ω_ϕ and Ω_θ are close enough to $\Omega_{\rm H}$ to suppress the most important modes of the tide. On the right, we we show the amplitude of C_+ as a function of a, showing how strongly this field varies thanks to this proportionality of the modes with p_Λ.

of Fig. 4) and $a = 0.9M$, $p = 3.5M$, $e = 0.7$ (bottom-right panel) both demonstrate significate deviations from this prototype. Consider the $a = 0.3M$ case first: the spike at periapse passage in this case is interrupted by about a cycle and a half of very small amplitude wiggle. This phenomenon appears to arise because of a change in the relative angular speeds of the orbit and of the event horizon during periapse passage.

To understand this, recall (as discussed in paper I) that the tidal field Ψ_0 (and hence C_+) vanishes for orbits that co-rotate with the event horizon. This only occurs for circular, equatorial orbits, and is simple to understand: such orbits are characterized by only one frequency, Ω_ϕ, and so $\omega_{mkn} \to m\Omega_\phi$. If $\Omega_\phi = \Omega_{\rm H}$, then $p_\Lambda = m(\Omega_\phi - \Omega_{\rm H}) = 0$, and by Eq. (2.29) $\Psi_0 = 0$.

In our case, the orbit does not co-rotate with the horizon for all time, but it co-rotates at two moments as it moves through periapsis. The top panel on the right of Fig. 4 shows $d\phi/dt$ near periapse passage, comparing it to the horizon's spin frequency $M\Omega_{\rm H}$. The orbit's angular speed is slower than the horizon's spin until $v \simeq 315.9M$. It is then faster than the horizon until $v \simeq 346.3M$, returning to a slower angular speed than the horizon. The small-scale oscillations in C_+ occur almost precisely during the moments that the orbit overtakes the hole's rotation. The tidal field oscillates with small amplitude as the orbit passes through co-rotation and back near its

periapse passage.

The additional oscillations we see in the periapse spike for the case $a = 0.9M$, $p = 3.5M$, $e = 0.7$ are simpler to explain. This orbit has a "zoom-whirl" structure, in which the small body "whirls" multiple times around the event horizon at periapsis before "zooming" back to apoapsis. The bottom panel on the right of Fig. 4 shows the number of windings about the horizon, $\phi/2\pi$, that the orbit executes as a function of time. The orbit winds the horizon about two and a half times in the time interval $180M \lesssim v \lesssim 230M$ (periapsis occurs at $v = 203M$, near the middle of this range). The multiple oscillations in C_+ occur during the period in which the orbit is whirling close to the black hole.

C. Summary of tidal behavior

We conclude our discussion of the tide by summarizing the features that we found above. For the most part, we find that the dynamics of the fields $C_{+,\times}$ correlate with the dynamics of the orbit. For circular orbits, the tides are essentially sinusoidal, with the amplitude modulated by the axial angle at which the field is measured. Thanks to frame dragging, for the Kerr case this modulation becomes associated with the orbit, leading to a dynamical
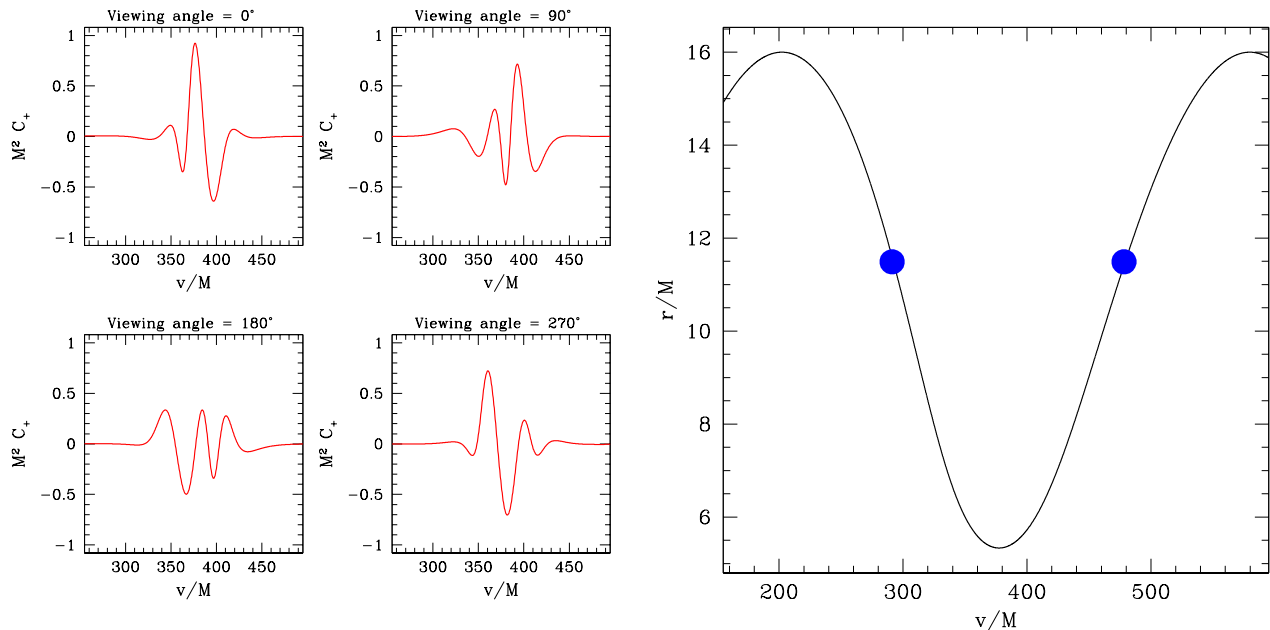
FIG. 3: Examples of the on-horizon tidal field C_+ for an eccentric equatorial orbit of a Schwarzschild black hole (left), and a portion of that orbit's radial motion (right). The orbit has $p = 8M$, $e = 0.5$. We examine C_+ on the hole's equator at four different axial positions. (We don't show the cross polarization since $C_\times = 0$ at $\theta = 90°$ for tides from equatorial orbits.) Consider first the tidal field at $\psi = 0°$. The shape of this field can be considered a prototype of the tide from an eccentric orbit: There is a large spike at roughly the moment the orbit passes through $r = r_{\min}$, with smaller scale oscillations before and after. The oscillations and spike occur only when the orbit is close to the event horizon. In the right-hand panel, we have marked with large dots the moments when the orbital radius is $r = 10^{1/3} r_{\min}$. Since the tide scales roughly as $1/r^3$, these should indicate when the tide has fallen by about an order of magnitude from its peak value. Indeed, at these moments ($v \simeq 295M$ and $v \simeq 475M$) the tide has fallen by at least an order of magnitude. The three other small panels on the left-hand side illustrate how the tide is modulated by azimuth angle. The position at which the field is measured can significantly affect the qualitative appearance of the tide during periapse passage.

modulation of the tide's amplitude.

For eccentric orbits, the prototype form of the tide is a large spike at periapse passage, modulated by the axial angle in a manner similar to the axial modulation we saw with circular orbits. "Zoom whirl" orbits, fairly common in the strong field of rapidly spinning black holes, are orbits in which the orbit "whirls" around the black hole at periapsis, completing multiple revolutions before "zooming" back out to apoapsis. In such cases, multiple oscillations occur during the large amplitude periapse spike.

Certain interesting and seemingly subtle features of the tides we find originate in the fact that modes of the tidal field are proportional to $p_\Lambda = \omega_\Lambda - m\Omega_{\rm H}$. This factor varies quite a bit depending on the hole's spin and the nature of the orbit. This leads to substantial variation in the amplitude of the tide when we consider a sequence in which the orbit's geometry is held fixed and the black hole spin is varied. It also leads to interesting behavior when we consider orbits for which $\omega_\Lambda \simeq m\Omega_{\rm H}$.

Figure 5 shows how the features of tides from inclined circular and equatorial eccentric cases combine for generic orbits. We examine two orbits with $p = 8M$, $\theta_{\rm inc} = 60°$ about a black hole spin $a = 0.6M$. One orbit has eccentricity $e = 0.2$, the other $e = 0.5$. The low ec-

centricity case blends the features of the inclined circular and equatorial eccentric limits in fairly straightforward way: we find relatively high amplitude tidal spikes at each periapse passage, with sinusoidal tidal oscillations between each passage. In the case $e = 0.5$, the behavior we see practically cannot be distinguished from an equatorial eccentric case. The eccentricity is sufficiently large in this case that there is a very large contrast between the tidal spike near periapse and the much weaker tide at apoapsis. Any oscillations between periapse passages are dwarfed by the much more important spike in the tide when the orbit is closest to the black hole.

IV. HORIZON DYNAMICS I: CONSISTENCY TEST FOR THE SCHWARZSCHILD LIMIT

We now turn to our examination of the dynamics of the horizon's geometry. We begin by first testing whether the Schwarzschild limit exhibits the correct behavior. These black holes are spherically symmetric, so there is no physical distinction between an equatorial orbit ($\theta_{\rm inc} = 0°$) and an orbit of arbitrary inclination. Our representation of these orbits will certainly be different, but this is due
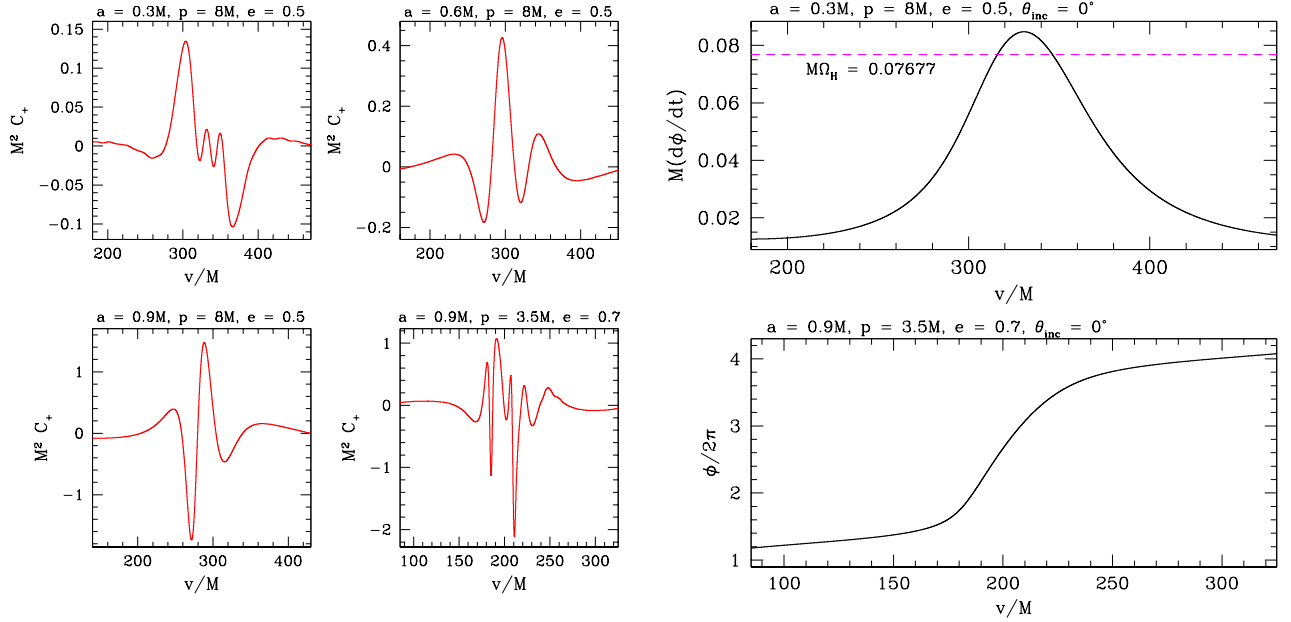
FIG. 4: Examples of the on-horizon tidal field C_+ for equatorial eccentric orbits of Kerr black holes (left), and features of the orbits which we use to explain some of the behavior we find (right). The cases shown here demonstrate several examples of interesting behavior for strong-field Kerr orbits. On the left, the top panels and the bottom left panel are for orbits with $p = 8M$, $e = 0.5$, and show orbits about black holes with spins $a = 0.3M$, $a = 0.6M$, and $a = 0.9M$; the bottom right panel on the left is for an orbit with $p = 3.5M$, $e = 0.7$ about a black hole with $a = 0.9M$. In all cases, we examine the field at $\theta = 90°$, $\psi = 0°$; $C_\times$ vanishes there for all equatorial orbits. The behavior we see in the top-right and bottom-left panels is very similar to the prototype behavior of C_+ we saw in Fig. 3: a large spike coinciding with periapse passage, and smaller-scale oscillations before and after. The behavior we see in the top-left and bottom-right deviates from the prototype in interesting ways. For $a = 0.3M$, $p = 8M$, $e = 0.5$, C_+ undergoes additional very small-amplitude oscillations during the spike. On the right, the top panel compares the orbit's axial speed $d\phi/dt$ with the horizon's spin frequency $\Omega_{\rm H}$. The small amplitude oscillations occur during the brief span in which $d\phi/dt$ exceeds $\Omega_{\rm H}$. For $a = 0.9M$, there are multiple high-amplitude oscillations near the largest spike. This is correlated with "whirling" orbital dynamics. As shown in the bottom panel on the right, the orbit wraps around the black hole multiple times at periapsis before "zooming" back out to apoapsis.

to the coordinate orientation we have chosen. (By contrast, when $a \neq 0$, the black hole's spin axis picks out a preferred spatial direction.) We thus expect that many properties related to black hole perturbations should become invariant with respect to orbit inclination for $a = 0$, or else vary in a simple way.

This limiting behavior has been discussed in past work, in particular describing how the amplitude of gravitational waves and the energy that they carry varies as the orbit's inclination varies. As one example, consider the energy carried by gravitational waves. The total energy carried by a given l-mode must be constant as a function of orbital inclination:

$$\left(\frac{dE}{dt}\right)_l \equiv \sum_{mkn} \left(\frac{dE}{dt}\right)_{lmkn}$$
$$= \text{constant with } \theta_{\rm inc} \; . \qquad (4.1)$$

The sum in Eq. (4.1) is taken over m from $-l$ to l, and over n from $-\infty$ to ∞. The sum over k in principle runs from $-\infty$ to ∞, though many modes do not actually contribute, as we discuss momentarily.

Although the summed flux $(dE/dt)_l$ does not vary with $\theta_{\rm inc}$, the distribution of gravitational-wave power among the harmonic indices varies with inclination quite a bit. In the Schwarzschild limit, $\Omega_\theta = \Omega_\phi$. Consider two orbits which are identical except for inclination. One is equatorial ($\theta_{\rm inc} = 0°$), the other is not. Power in an axial m-mode at $\theta_{\rm inc} = 0°$ becomes distributed among polar k-modes and axial modes with $m' = (m - k)$ in the inclined orbit. The way in which the power is so distributed is easily deduced from the rotation properties of spherical harmonics:

$$\frac{(dE/dt)_{l(m-k)kn}(\theta_{\rm inc})}{(dE/dt)_{lm0n}(\theta_{\rm inc} = 0°)} = \left| \mathcal{D}^l_{(m-k)m}(\theta_{\rm inc}) \right|^2 \; . \qquad (4.2)$$

Here, $\mathcal{D}^l_{(m-k)m}$ is a Wigner function, which relates the spherical harmonic Y_{lm} at θ to the harmonic $Y_{l(m-k)}$ at $\theta - \theta_{\rm inc}$. (This relation implies that there is no power in any mode with $|m + k| \geq l$.) Further discussion of this relation is given in Refs. [11] (with a few minor errors) and [21] (which corrects those errors).

What applies to the gravitational wave flux likewise applies to all the quantities which describe tidal distor-
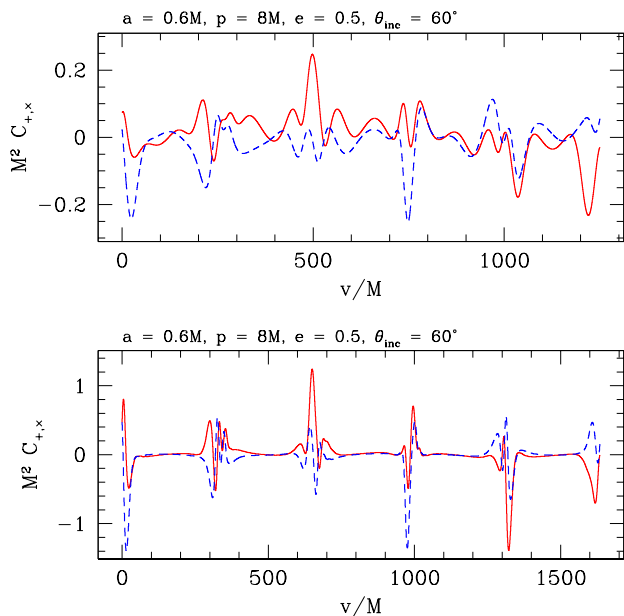
FIG. 5: Example of the on-horizon tidal polarizations $C_{+,\times}$ for generic Kerr orbits. Both panels show the tide for orbits with $p = 8M$, $\theta_{\rm inc} = 60°$ about black holes with spin $a = 0.6M$; top is for an orbit with the relatively low eccentricity $e = 0.2$, bottom is for the much larger value $e = 0.5$. The solid (red) curves show C_+, and the dashed (blue) curves show $C_\times$. In both cases, we show the tide resulting from five complete radial cycles of the orbit's motion. For $e = 0.2$, we see a blending of features of the circular inclined and eccentric equatorial tides, with larger amplitude spikes occuring near periapse passage, and sinusoidal oscillations between these spikes. For $e = 0.5$, the behavior is dominated by the very large spike seen at periapse passage, and is quite similar in form to the eccentric equatorial case.

tions of a Schwarzschild black hole's event horizon. We find that, in all cases we have checked, quantities transform under rotation exactly as they should. This is not terribly surprising, since this property of our code has been checked very carefully in previous analyses. It is reassuring, however, that the modifications we have made to compute the horizon's tidal distortion have not broken this behavior.

Figure 6 shows one example of a test for the rotational consistency of Schwarzschild horizon distortions. Consider two orbits around a Schwarzschild black hole, both with $p/M = 10$ and $e = 0.5$. One orbit is equatorial in the coordinates we impose, the other is highly inclined ($\theta_{\rm inc} = 80°$) in these coordinates. Due to spherical symmetry, the horizon distortion for the equatorial case should be identical to the horizon distortion in the inclined case, correcting for the tilt of $\theta_{\rm inc}$.

In this figure, we show the perturbation to the radius of the horizon's embedding surface, $r_{\rm E}^{(1)}$, for these two cases. The solid (blue) line shows the distortion for the inclined case as measured at $\psi = 0$, $\theta = 10°$ (i.e., rotated $\theta_{\rm inc}$
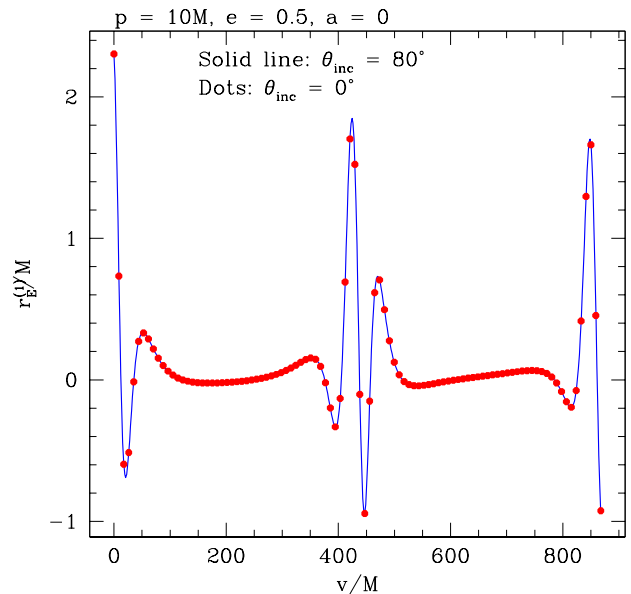

FIG. 6: A test for consistency of our results in the $a = 0$ limit: the distortion to the embedded horizon arising from a highly inclined orbit [$\theta_{\rm inc} = 80°$; solid (blue) curve] as measured by an observer sitting $\theta_{\rm inc}$ above the equator, and from an equatorial orbit [$\theta_{\rm inc} = 0°$; points (red)] as measured by an observer on the equator. Both data sets include modes to $l = 7$; we estimate that contributions beyond this affect the horizon's shape at a level $r_{\rm E}^{(1)}/2M \lesssim 10^{-7}$. The two data sets agree to within numerical accuracy, as they should — a Schwarzschild black hole is spherically symmetric, so there is no unique notion of the hole's equator.

from the equator). The dots (red) show the distortion at $\psi = 0$ on the equator for the equatorial orbit. We include all modes which contribute to the horizon's distortion up to $l = 7$; we estimate that modes beyond this affect the horizon's shape at a level $r_{\rm E}^{(1)}/2M \lesssim 10^{-7}$.

Although these calculations were done using very different orbits, and very different modes enter the expansion, the horizon distortions $r_{\rm E}^{(1)}$ we find are essentially identical, only differing due to accumulated round-off error at a level $\lesssim \epsilon$, where $\epsilon \simeq 10^{-10}$ is a parameter controlling the accuracy of numerical integrals. If both curves had been plotted as solid lines, they would have been indistinguishable here. This is a typical example of how our code handles this consistency test.

V. HORIZON DYNAMICS II: APPLIED TIDAL FIELD AND RESULTING SHEAR

We begin with an analysis of the horizon's response to an equatorial, eccentric orbit. The applied tidal field varies from quite strong near periapsis [$r = r_{\rm min} = p/(1+e)$] to weak near apoapsis [$r = r_{\rm max} = p/(1-e)$], giving
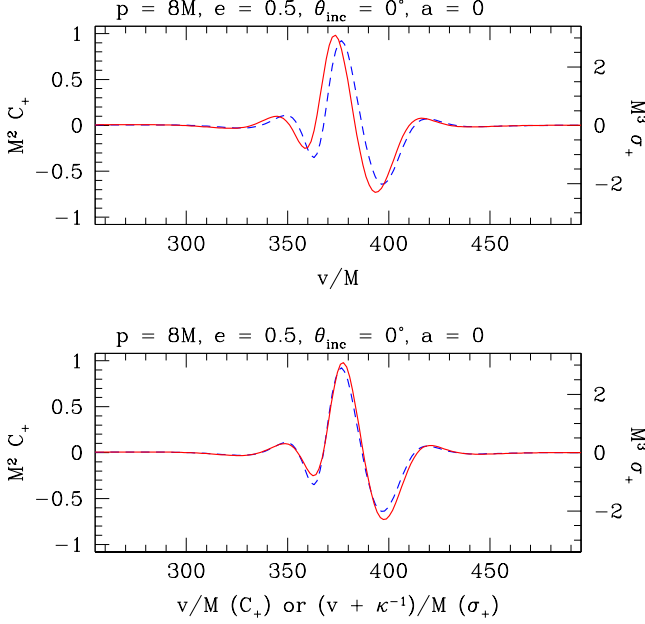
FIG. 7: Applied tidal field versus shear response for an eccentric equatorial orbit of a non-spinning black hole. Data are for an orbit with $p = 8M$, $e = 0.5$, $\theta_{\rm inc} = 0°$. We show the on-horizon Weyl curvature polarization C_+ [dashed (blue) curves], as well as the resulting shear polarization σ_+ [solid (red) curves]. Both fields are plotted at $\theta = 90°$, $\psi = 0°$, and include all modes up to $l = 9$. The top panel shows C_+ and σ_+ as functions of ingoing time v. Notice that σ_+ appears to lead C_+ by an almost constant time interval. The bottom panel shows the same data, but with σ_+ shifted by $\Delta v = \kappa^{-1} = 4M$. The shear response lines up almost perfectly with the driving tide in this panel, showing that the shear σ_+ leads the tide by κ^{-1} in the Schwarzschild limit.

us a chance to study the horizon's response for a wide range of applied tidal field.

A. Relative phase of the tide and shear

We begin our study of the shear induced on the horizon by examining its phase relative to the driving tide. In paper I, the driving tide was stationary, and the difference between the tide and the response amounted to a simple phase shift. For generic orbits, the difference is not so simple.

Figures 7, 8, and 9 compare the tidal field and shear in five different situations. In all cases, the orbit has $p = 8M$, $e = 0.5$, $\theta_{\rm inc} = 0°$, but the black hole spin varies over $a/M \in [0, 0.3, 0.6, 0.9, 0.9999]$. We include all modes up to $l = 9$ in these plots. We compare one polarization of the on-horizon Weyl tensor, C_+ [dashed (blue) curves], to the corresponding polarization of the horizon's shear, σ_+ [solid (red) curves]. The orbits are all equatorial, so we examine these quantities in the holes' equatorial planes: all data are shown at the point $\theta = 90°$, $\psi = 0°$.
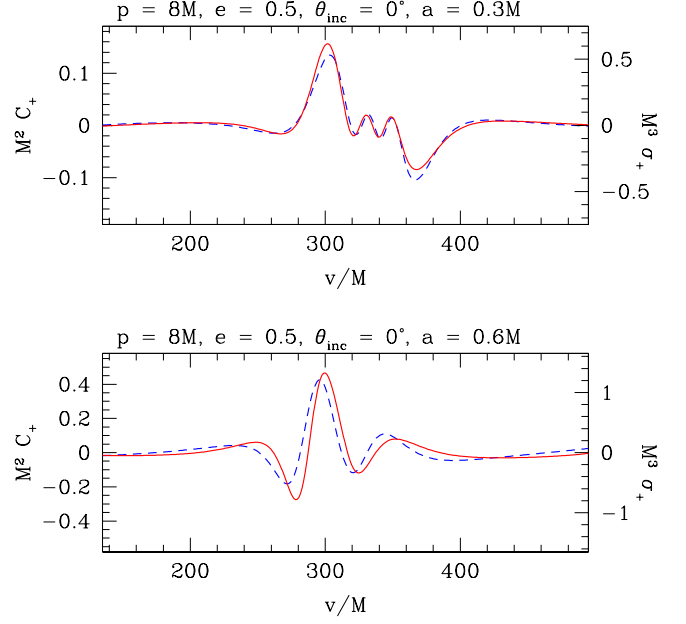
FIG. 8: Applied tidal field versus shear response for eccentric equatorial orbits of spinning black holes. Data in both panels are for an orbit with $p = 8M$, $e = 0.5$, $\theta_{\rm inc} = 0°$, and include modes up to $l = 9$. Top is for a hole with spin $a = 0.3M$, bottom for $a = 0.6M$. As in Fig. 7, we show the on-horizon Weyl curvature polarization C_+ [dashed (blue) curve] and the shear polarization σ_+ that results [solid (red) curve]. All data are plotted at $\theta = 90°$, $\psi = 0°$.

Begin with Fig. 7, which shows C_+ versus σ_+ for orbits of a Schwarzschild black hole. The top panel of this figure shows that the horizon's response leads the driving tide by what is apparently a constant offset. To understand this, consider again Eq. (2.34):

$$\frac{\sigma_\Lambda}{\Psi_{0,\Lambda}} = \frac{\exp\left[-i\arctan(p_\Lambda/\kappa)\right]}{\sqrt{p_\Lambda^2 + \kappa^2}} \ . \tag{5.1}$$

In the Schwarzschild limit, $p_\Lambda = \omega_\Lambda$, and $\kappa^{-1} = 4M$. Each mode σ_Λ of the shear response leads the driving tide Ψ_0 by $4M\omega_\Lambda$ radians. This is equivalent to σ leading Ψ_0 in time by $4M$. We check this in the bottom panel of Fig. 7: this plot is identical to the top panel of Fig. 7, but we have shifted σ_+ by $\Delta v = \kappa^{-1} = 4M$. Notice that the tide and the shear are almost precisely aligned in this panel, confirming that the responses here differ primarily by a temporal offset of $\kappa^{-1} = 4M$.

As the black hole's spin increases, the shift between the applied tide and the shear response becomes more complicated: the timescale κ^{-1} becomes larger as $a \to M$, and the wavenumber $p_\Lambda = \omega_\Lambda - m\Omega_{\rm H}$ which enters the mode ratio (2.34) differs significantly from the frequency ω_Λ. We can see the impact of this change in Fig. 8. In the top panel, we examine C_+ and σ_+ for the same orbit used in Fig. 7 ($p = 8M$, $e = 0.5$, $\theta_{\rm inc} = 0°$), but now about a black hole with spin $a = 0.3M$. In this case, the tide and
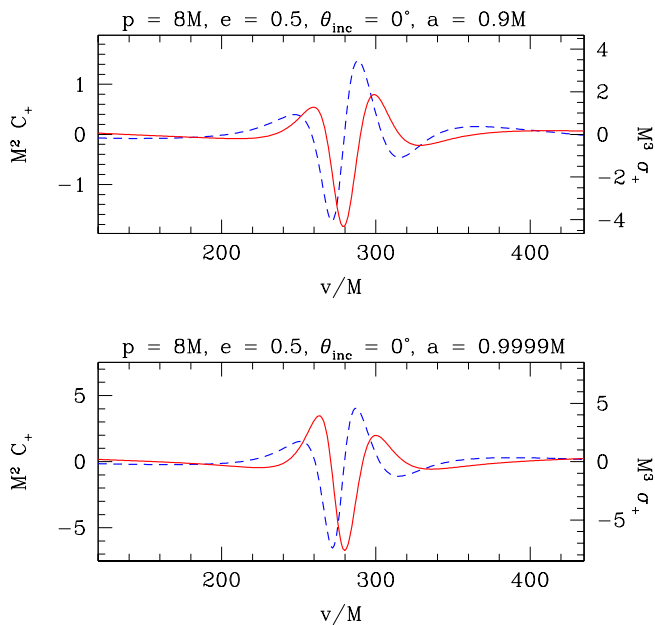
FIG. 9: Applied tidal field versus shear response for eccentric equatorial orbits of spinning black holes. Data in both panels are for an orbit with $p = 8M$, $e = 0.5$, $\theta_{\rm inc} = 0°$, and include modes up to $l = 9$. Top is for a hole with spin $a = 0.9M$, bottom for $a = 0.9999M$. As in Figs. 7 and 8, we show the on-horizon Weyl curvature polarization C_+ [dashed (blue) curves] and the shear polarization σ_+ that results [solid (red) curves]. All data are plotted at $\theta = 90°$, $\psi = 0°$.

the shear are nearly coincident as a function of ingoing time v (including the small-amplitude oscillations in the periapse spike we discussed in Sec. III). In the bottom panel, we plot C_+ and σ_+ for this orbit about a black hole with spin $a = 0.6M$. The tide now leads the shear, and the shapes are not congruent. Empirically, we find that if we shift σ_+ by $\delta v \simeq 3.8M$ we can make the largest peaks line up. Other features, however, do not line up so well; the differing behaviors of C_+ and σ_+ cannot be ascribed to a simple time shift.

The trend seen in Fig. 8 continues in Fig. 9, which shows C_+ and σ_+ for the same orbit about black holes with $a = 0.9M$ (top) and $a = 0.9999M$ (bottom). We again see that the tidal field C_+ leads the shear response σ_+. We can match the largest peaks by shifting σ_+ by $\delta v \simeq 8M$ in the case $a = 0.9M$, and by $\delta v \simeq 9M$ in the case $a = 0.9999M$. However, none of the other features align when we do this, indicating that the shift at these large spins cannot be described as a simple shift in time.

One interesting feature that comes across as we review Figs. 7 – 9 is the transition from shear leading the tide at $a = 0$ to shear lagging the tide for $a > 0.3M$. This transition is reminiscent of the behavior of the tidal bulge that was seen in paper I. There, we found for circular equatorial orbits that the tidal bulge leads the applied tide at small spin, and lags the applied tide at large spin. At least in the small a and large a limits, this could

be understood in the circular equatorial case as reflecting the relative angular frequencies of the orbit and the black hole. Qualitatively similar behavior clearly shows up for these dynamical situations, although quantifying it is not so straightforward since these orbits have a more complicated time-frequency structure.

B. High-frequency oscillations at high spin

At the highest spins we have examined, a new phenomenon emerges: a high-frequency oscillation in the shear σ following the orbit's passage through periapsis. This oscillation decays over a time of about $70M$ for the orbits we have examined. An example is shown in Fig. 10. Both panels of this figure show data for equatorial orbits with $e = 0.7$ about black holes with spin $a = 0.9999M$. The left panel shows data from an orbit with $p = 10M$. The behavior of C_+ and σ_+ is quite similar to the cases discussed previously: C_+ shows a large spike near periapse passage, with small scale oscillations before and after; σ_+ has a similar shape, offset somewhat in time. (Because this is an equatorial orbit and we examine these fields on the equator, $C_\times$ and $\sigma_\times$ are both zero.)

On the right, we show a much stronger field orbit, $p = 3M$. The spike at periapse passage has several large amplitude oscillations characteristic of the "whirling" near periapsis common for large spin, strong-field orbits. This is essentially the same phenomemon seen in the bottom-right panel on the left-hand side of Fig. 4. The new phenomenon to which we call attention are the low-amplitude, high-frequency wiggles that follow periapse passage. We see roughly seven low-amplitude cycles in σ_+ between periapse spikes, decaying in amplitude as the system evolves from one spike to the next. These wiggles are only apparent in the shear σ_+; we have not seen evidence of them in the tidal field C_+.

As we complete this analysis, the origin of these low-amplitude oscillations is a mystery. They do not appear to be a numerical artifact; we are confident that our harmonic expansion has converged, as including additional modes does not change our results beyond the ninth or tenth digit. The fact that these oscillations only appear in the shear σ_+ and not in the tidal field C_+ or Ψ_0 indicates that they cannot be related to the hole's quasi-normal modes. As we'll discuss in a moment, the behavior of their decay also argues against such an explanation. In an earlier version of this paper, we argued that these wiggles could be understood as an imprint of the teleological Green's function discussed in Sec. II B, with the oscillation frequency related to the horizon's spin frequency $\Omega_{\rm H}$, and the decay to the Green's function's decay time $\kappa^{-1} = 2r_+/\sqrt{1 - (a/M)^2}$. On deeper analysis (prompted by our original submission's referee report), we have concluded that the data does not support this explanation either.

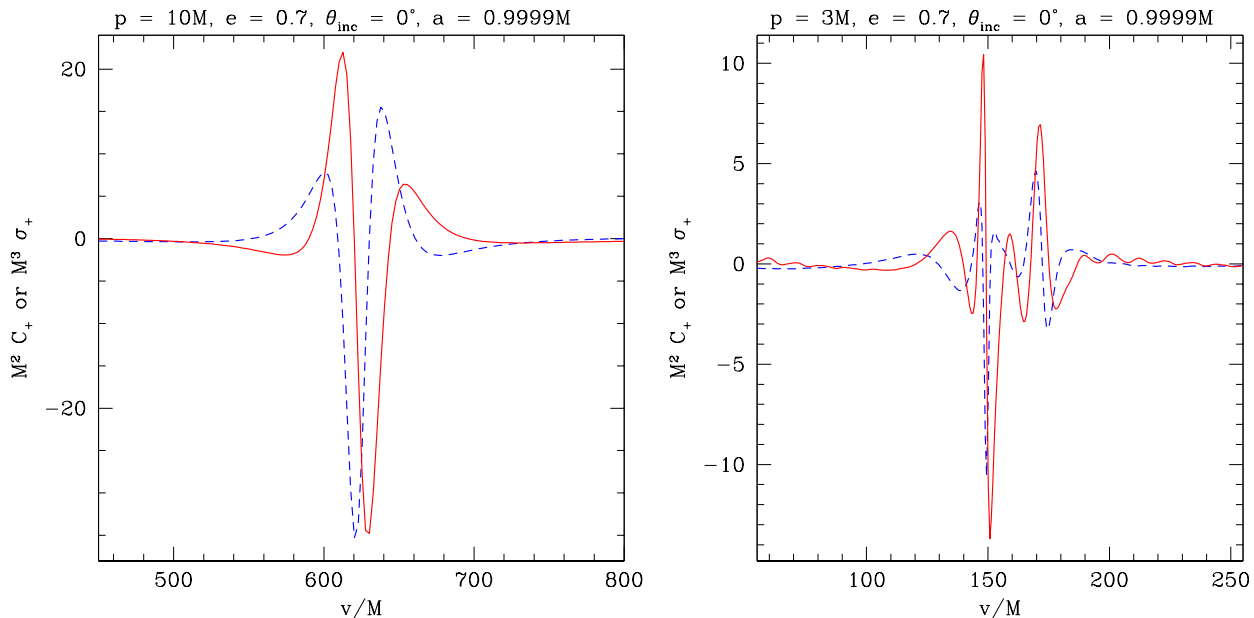For now, rather than offering any hypotheses attempting to explain these wiggles, we simply lay out the empir-

FIG. 10: Detailed study of the horizon's shear response σ_+ [solid (red) curves] given a driving tidal field C_+ [dashed (blue) curves] for the case of very rapid spin, $a = 0.9999M$. In both panels, we consider equatorial ($\theta_{\text{inc}} = 0°$) orbits with eccentricity $e = 0.7$, and include all modes up to $l = 9$. In the left-hand panel, the orbit has semi-latus rectum $p = 10M$; in the right, $p = 3M$. For the case $p = 10M$, no particularly noteworthy feature is evident. This behavior is qualtitatively similar to the shear response that we see across a wide range of orbits: σ has a shape similar to C, but is offset as a function of time. However, for high spins and strong-field orbits, new behavior emerges: low-amplitude, high-frequency wiggles can be seen in the shear between the high-amplitudes "bursts" corresponding to the orbit's periapse passage. Notice that these wiggles are not present in the tidal field, only in the shear response.

ical situation as it stands. Figure 11 zooms in on the region of Fig. 10 in which this phenomenon is apparent. We also include data for additional spin values for orbits with this geometry. The trend we see is that the frequency of the oscillations is nearly the same for these cases, evolving slightly as the spin moves toward the extremal limit. The decay time likewise is nearly constant over this range of spin. The near constancy of the decay time appears to rule out an explanation for these wiggles based on black hole quasi-normal modes, or on the Green's function (2.39). Both of these explanations would require the decay time to become dramatically longer as $a \to M$. The form of the teleological Green's function, for example, would lead us to expect the decay time to increase by a factor of ten as the spin changes from $a = 0.9999M$ to $a = 0.999999M$. The lack of such increase points to some other mechanism.

By fitting and subtracting a quadratic to remove the secular trend in the data shown in Fig. 11, we can more accurately locate the position of the peaks and estimate the frequency associated with the wiggles. Assuming that the phase of these wiggles follows the form

$$\Phi_{\text{wiggle}} = \Omega_{\text{wiggle}}v + \delta\Phi \qquad (5.2)$$

and requiring that the phase of the peaks lie on the line

$$\Phi_{\text{wiggle}}(\text{peak}) = 2\pi n \qquad (5.3)$$

a/M	$\sqrt{1-(a/M)^2}$	$M\Omega_{\text{wiggle}}$	$M\Omega_{\text{H}}$	$M\Omega_\phi$	$M\Omega_r$
0.9995	0.03162	0.5826	0.4844	0.0988	0.0399
0.9999	0.01414	0.5805	0.4930	0.0988	0.0399
0.99999	0.004572	0.5792	0.4978	0.0988	0.0399
0.999999	0.001414	0.5787	0.4993	0.0988	0.0399

TABLE I: The best-fit frequency Ω_{wiggle} characterizing the high-frequency oscillations shown in Fig. 11. We present this frequency as a function of both the black hole spin a/M, and the parameter $\epsilon \equiv \sqrt{1-(a/M)^2}$ which characterizes deviation from extremality. For comparison, we show the hole's spin frequency Ω_{H} for these spins, and the orbit's geodesic frequencies Ω_ϕ and Ω_r. We see no obvious physically motivated way to connect Ω_{wiggle} to these other frequencies.

with n integer, we can estimate the wiggle frequency that best fits our data. The results are summarized in Table I. We present the best-fit frequencies versus both the spin a and a parameter $\epsilon \equiv \sqrt{1-(a/M)^2}$, which characterizes the deviation of the spacetime from extremal Kerr.

We find that a linear fit in ϵ describes our best fit frequencies quite well. Performing a least-squares fit of our data, we find

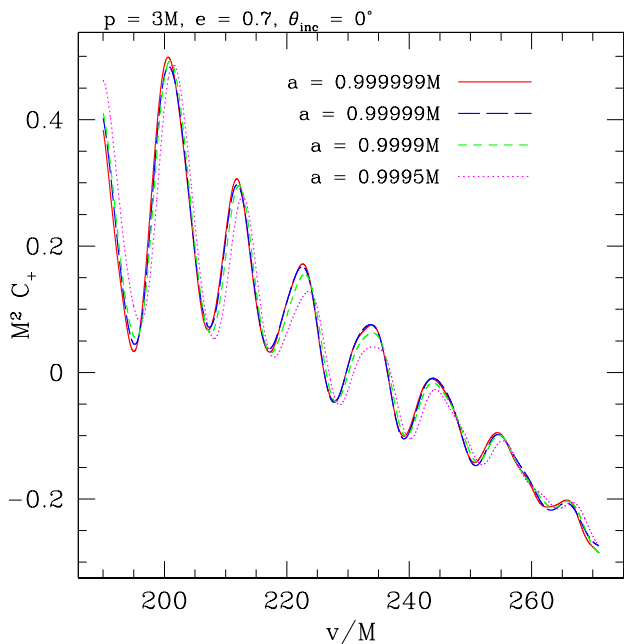$$M\Omega_{\text{wiggle}} = (0.5786 \pm 0.0001) + (0.1288 \pm 0.0032)\,\epsilon\,. \qquad (5.4)$$

FIG. 11: A zoom on the high-frequency wiggles shown in the right-hand panel of Fig. 10. Along with the $a = 0.9999M$ case shown previously, we include data describing wiggles for orbits with the same values of p, e, and θ_{inc}, but for spins $a = 0.9995M$, $a = 0.99999M$, and $a = 0.999999M$. As described in the text, the frequency associated with the wiggles (which we have not succeeded in relating to other frequencies in the problem) decreases slightly as a function of spin. The rate at which the amplitude decays does not vary significantly with spin. We have not been able to come up with a satisfactory explanation for the phenomenon of these wiggles.

Although the goodness of this fit with ϵ is intriguing, we cannot yet claim any understanding for what this might signify. In Table I, we include the geodesic frequencies Ω_ϕ and Ω_r for the orbits used in Fig. 11, as well as the horizon frequency Ω_{H}. As an exercise in arithmetic, we can find no combination of these frequencies that produces the values we find for Ω_{wiggle}. Absent any compelling physical model, any combination we did find would arguably be no more useful than numerology.

For now, we leave this phenomenon as an intriguing empirical finding of this analysis, and hope that additional work may explain it in the future.

VI. HORIZON DYNAMICS III: HORIZON EMBEDDINGS

In this section, we examine dynamical horizon embeddings for several representative orbits. Our goal will be to show how the horizon behaves as a function of the orbit's behavior, so we will show a sequence of figures that show both the tidally distorted horizon and the smaller member of the binary. As discussed at length in paper I, there is substantial ambiguity in such a plot, associ-

ated with the fact that the horizon and the orbit are at different positions in a curved spacetime. Comparing the horizon and the orbit requires that we carefully define exactly what is shown. Following the choices that we made in paper I, our plots are all shown on a slice of constant ingoing time v; this is equivalent to what we called the "instantaneous map" in paper I.

One might wonder why, given this ambiguity, we choose to present our data using these embedding diagrams. Indeed, there are multiple ways that one can present data representing the geometry of distorted black holes. For example, one could make a color map representing the scalar curvature $R_{\text{H}}^{(1)}$, or a color map representing the phase between the on-horizon tide Ψ_0 and the resulting shear σ. (Note that both Ψ_0 and σ are spin-weight 2 quantities, and so cannot be simply represented on a surface — both, for example, are multiply valued at the poles, $\theta = 0$ and $\theta = \pi$.) Such representations have the advantage of presenting quantities that are less ambiguious.

In the end, we have chosen to use embeddings primarily for aesthetic reasons. One of our goals was to develop graphics which demonstrate the extent to which a black hole's shape was distorted by tides from its companion. Although one must be careful in interpreting this shape, embeddings provide a compelling picture of this tidal shape distortion. We supplement the shape with a color map which codes the horizon's distortion from the shape it would have in the absence of a binary companion. In all of the figures which follow, surfaces colored green are essentially undistorted from the embedding of an isolated black hole; those colored red have larger radius than that of an isolated black hole; and those colored blue have smaller radius. We find that color maps of other quantities, such as the scalar curvature $R_{\text{H}}^{(1)}$ are visually quite similar to the color maps we associate with the embedding. For our purposes, horizon embeddings, though somewhat arbitrary, convey exactly the information that we hoped to present. Using the tools we have developed here and in paper I, it is straighforward to modify this analysis to focus upon other measures of horizon distortion.

As in paper I, a major shortcoming of our use of embeddings is that we embed the horizon in a Euclidean three-dimensional space. This means we are confined to spin parameter $a/M \leq \sqrt{3}/2$; for faster spins, even an undistorted horizon cannot be embedded in this geometry. As mentioned previously, work in progress indicates that embedding the horizon in the globally hyperbolic space H^3, following Ref. [32], is an elegant way to get around this restriction.

The cases we examine in detail are associated with Figs. 12 – 15. These figures are each a series of snapshots taken from animations showing the combined orbital and embedded horizon dynamics. These animations are available at [28]. Readers may find it useful to examine these visualizations in concert with the text presented below.

A. Embeddings from inclined circular orbits

We begin with an especially simple case: an inclined, circular orbit of a Schwarzschild black hole. Figure 12 shows an embedding of the distorted horizon for the case of a circular orbit with radius $r = 6M$ inclined at $\theta_{\rm inc} = 60°$. We show 12 frames illustrating the horizon embedding and particle motion for this orbit; the frames are evenly spaced over nearly one orbital period ($T_{\rm orb} = 92.3M$ for a circular orbit at $r = 6M$ for Schwarzschild). Axes indicate the location of the equatorial plane; they are static in this sequence, since the horizon of a Schwarzschild black hole is static. The bottom two panels of this figure show the angular position of the horizon's bulge [defined as the coordinate for which the embedding radius is largest; dotted (blue) curves] and the orbiting body [solid (red) curve], both as functions of ingoing time v. Bottom left panel shows $\cos\theta(v)$; bottom right shows $\psi(v) - \Omega_\phi v$. (We subtract $\Omega_\phi v$ to remove an uninteresting overall secular growth in ψ over an orbit.)

As should be expected following Sec. IV, the results we see in Fig. 12 are consistent with the fact that the physics of an inclined orbit is identical to that of an equatorial orbit in the $a = 0$ limit. In particular, the embedded horizon is identical to that shown in the $r_{\rm orb} = 6M$ panel of paper I's Fig. 3, but with the distortion centered on a plane that is inclined at $\theta_{\rm inc} = 60°$ to our chosen equator. The offset between the orbit and the horizon's bulge is constant over the orbit, with the bulge leading the orbiting body by a fixed amount; this can be seen particularly clearly in an animation of the horizon and orbit dynamics, and in the plot of $\cos\theta(v)$. As we have previously discussed, this can be understood as due to the spherical symmetry of the Schwarzschild spacetime — the magnitude of the tidal field is constant over an orbit. In paper I, the lead was purely axial (i.e., purely in the direction of ψ); here it is a mixture of the axial and polar angles ψ and θ. As discussed extensively in paper I, bulge leading orbit is exactly what we expect for circular Schwarzschild orbits.

We next consider an inclined, circular orbit of a Kerr black hole. Circular Kerr orbits are defined as those for which the Boyer-Lindquist coordinate radius r is constant. Although they are therefore closely tied to a particular coordinate system, they nonetheless are a well-defined and well-studied subset of Kerr orbits. It has been shown that the eccentricity e of Kerr orbits [defined in Eq. (2.4)] decreases over all but the most strong-field orbits due to gravitational-wave driven backreaction [33, 34], and that orbits with $e = 0$ remain at $e = 0$ [35–37]. As such, we expect that gravitational-wave emission will drive large mass-ratio binaries toward the constant Boyer-Lindquist radius circular limit.

Figure 13 is much like Fig. 12, but for an orbit of a black hole with spin parameter $a = 0.6M$. The orbit again has constant radius $r = 6M$, and is inclined at $\theta_{\rm inc} = 60°$. We show 12 frames illustrating the horizon and particle motion for this orbit, with frames evenly spaced over nearly one orbital period[4]. In this sequence, the axes (which indicate the equatorial plane) are tied to the horizon's spin, which completes a full rotation in a period $T_{\rm H} = 2\pi/\Omega_{\rm H} = 37.7M$. The bottom two panels of Fig. 13 compare $\cos\theta$ and ψ for the horizon's bulge and the orbit's position.

Some new horizon dynamics begin to appear in Fig. 13. Over the course of an orbit, the tidal field arising from the small body is not of constant magnitude since the spacetime is no longer spherically symmetric. As a consequence the shape of the embedded horizon varies over an orbit. There is also interesting new behavior associated with the bulge-orbit offset. As discussed at length in paper I (and briefly in Sec. I), for circular, equatorial orbits of rapidly spinning black holes, the horizon bulge tends to lag the position of the orbiting body on a constant v timeslice. Let us call this "Kerr-like" bulge-orbit behavior, and let us call the opposite behavior (bulge leading the orbit on a constant v timeslice) "Schwarzschild-like." What we see in Fig. 13 is that the bulge behaves in a Kerr-like manner in the ψ-direction, but behaves in a Schwarzschild-like manner in the θ-direction. This can be seen by carefully examining the sequence of stills (and the animation from which these stills are taken), but is especially clear in the bottom two panels showing the angular position of the orbit and of the horizon's bulge.

We have found that this bulge-orbit behavior (Schwarzschild-like with respect to the θ direction, Kerr-like with respect to the ψ direction) is quite generic. It is clear in all the circular, inclined cases we have examined, and appears in inclined eccentric examples as well. This behavior arises from the fact that the black hole's spin picks out the ψ direction as special. The hole's rotation plus the horizon's teleological nature mixes time and axial angle: a tide that would produce a bulge on a Schwarzschild black hole at $(\theta_{\rm max}, \psi_{\rm max})$ will produce a bulge on a Kerr black hole at roughly $(\theta_{\rm max}, \psi_{\rm max} - \delta\psi)$, where $\delta\psi$ is (at leading order) proportional to the black hole's spin parameter a.

B. Horizon embeddings from eccentric orbits

We conclude our analysis by examining horizon embeddings for highly eccentric black hole orbits. The key point to bear in mind here is that, at leading order, the tidal field varies with orbital separation as $1/r^3$. As such, the tidal field from an orbit with eccentricity e varies by $(1 + e)^3/(1 - e)^3$ over the course of an orbit. This factor grows very quickly with e. The two cases we examine in

—————

[4] "Orbital period" is somewhat ambiguous for this orbit: the period to complete a single polar oscillation is $T_\theta = 98.7M$, and the period to complete a rotation of 2π radians in the axial direction is $T_\phi = 91.5M$. These two periods differ only by $\sim 10\%$, so our statement that we show nearly one period is accurate no matter which notion of period we use.
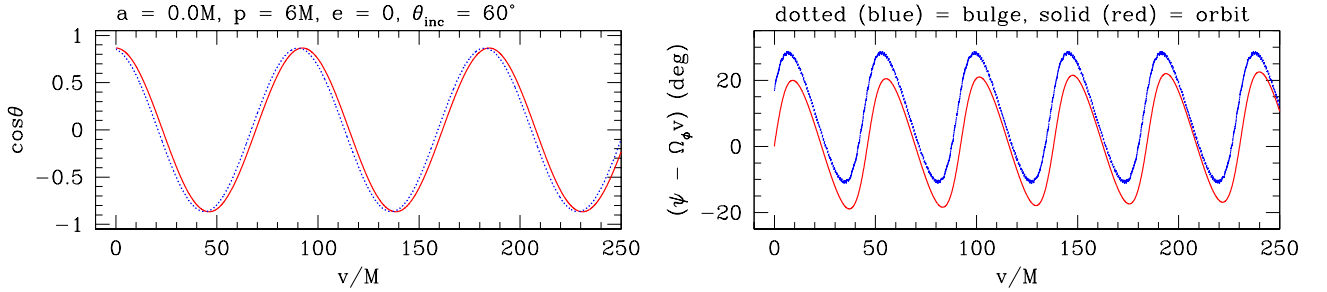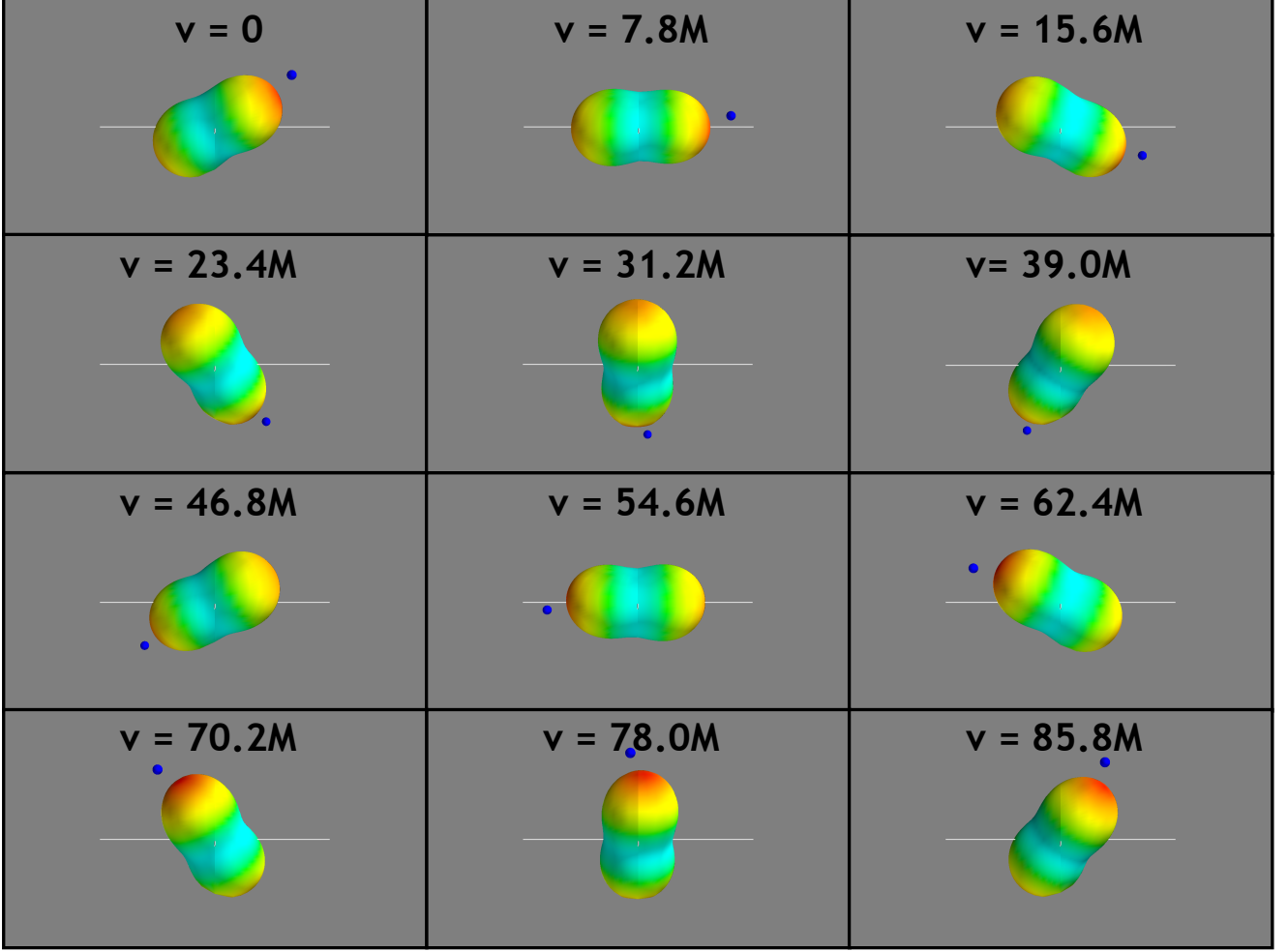
FIG. 12: Top: Snapshots of an animation depicting an embedding of the distorted horizon for a circular inclined orbit of a Schwarzschild black hole ($a = 0$). Bottom: Angular position of the horizon's bulge [dotted (blue) curve] versus the angular position of the orbiting body [solid (red) curve]. The orbit is at radius $r = 6M$, inclined at $\theta_{\text{inc}} = 60°$ to our chosen equatorial plane. The axes shown in these snapshots indicate the hole's equatorial plane; we have placed the camera slightly above this plane in order to illustrate the hole's bulge geometry. The orbiting body is indicated by the small "moon" (dark blue in color plot) located near one of the horizon bulges. The small body's orbit begins on the side of the black hole near the camera, descends down through the equatorial plane (crossing just after $v = 7.8M$), sweeps behind the far side of the hole (moving from right to left as plotted), then comes up through the equatorial plane (crossing just after $v = 54.6M$) to pass in front of the side near the camera again. The animation from which these stills are taken is available at [28]. The bottom two panels show the angular position of the bulge and the orbit, illustrating the polar angle ($\cos \theta$, left) and the axial angle (ψ, right). The horizon's bulge moves in lockstep with the orbiting body, always leading the orbit by a small, constant angle.

detail have $e = 0.7$, for which the tide varies by a factor of about 180. This means that the hole can be essentially unaffected by its companion for much of the orbit, but be highly distorted as the smaller body passes through periapsis.

Figure 14 shows this behavior quite clearly; see [28] for the animation from which these stills were taken. The large black hole used here has spin $a = 0.85M$, nearly the largest value for which a globally Euclidean embedding exists. The orbit is equatorial ($\theta_{\rm inc} = 0°$), quite strong field ($p = 4M$), and highly eccentric ($e = 0.7$). We only show a portion of a full radial cycle, from $r \simeq r_{\rm max}/2$ to $r_{\rm min} = p/(1 + e)$ back to $r \simeq r_{\rm max}/2$. As in Fig. 13, the axes indicating the equatorial plane rotate with the horizon. For $a = 0.85M$, the period of this rotation is $T_{\rm H} = 22.6M$. We sample our animation every $5.6M$. By coincidence, this is nearly $T_{\rm H}/4$, so the axes are sampled in a nearly stroboscopic fashion, and appear to be stationary.

The embedded horizon of an undistorted $a = 0.85M$ black hole is an oblate ellipsoid that is nearly flat at the poles. This geometry can be seen in the first and last few frames shown in Fig. 14 — the tidal field is so weak in these frames[5] (for which $r \sim r_{\rm max}/2$) that the horizon is not noticeably distorted by the companion. The distortion becomes quite strong as the orbital approaches periapsis: we see the horizon beginning to change shape at $v = 11.03M$, and is highly distorted over the range $22.06M \le v \le 33.10M$. At its peak, the horizon's distortion is similar to the most distorted horizon embedding shown in paper I, the right-hand panel of that paper's Fig. 7. Notice the Kerr-like bulge-orbit behavior: the bulge's position in ψ lags the orbit in all cases. This is quite clear in the $v = 27.58M$ panel, and in the plot of $\psi(v)$. (Since the orbit is equatorial, there is no lag or lead associated with θ.)

Notice also the high-frequency, low-amplitude wiggles in the ψ position of the horizon's bulge at $v \simeq 40M$ and $v \simeq 260M$. These are reminiscent of the high-spin features that we discussed in Sec. V B. In this case, we do not see such strong wiggles in the shear σ. It is plausible that the wiggles are present in σ, but at such low amplitude that they cannot be cleanly pulled out of that data; it could be that constructing other quantities associated with the horizon distortion, such as $R_{\rm H}^{(1)}$ and the embedding surface, makes the wiggles stand out even more strongly. Similar behavior is seen near periapsis for the generic case we discuss next (cf. lower right-hand panel of Fig. 15). We hope to study this further in future work.

Figure 15 shows the embedding for a horizon distorted by tides from a generic orbit. We again consider spin $a = 0.85M$, and a very strong-field ($p = 4M$), highly eccentric ($e = 0.7$) orbit, but we now take the orbit to be inclined at $\theta_{\rm inc} = 30°$. The set of frames we show again corresponds to motion from roughly $r_{\rm max}/2$ to $r_{\rm min}$ and back to nearly $r_{\rm max}/2$. We have moved the "camera" in this sequence to a point slightly above the equatorial plane in order to more clearly see the orbit's polar motion, and the distortions associated with motion above and below this plane.

The embedding dynamics shown in Fig. 15 combines the features found for inclined circular orbits with those found for eccentric equatorial orbits. In particular, notice that the embedded horizon geometry is practically undistorted in the first frame, as well as the last two or so frames. This again reflects the large range of the tidal field that acts on the horizon for eccentric orbits; when $r \gtrsim r_{\rm max}/2$, the horizon's distortions are so mild that they cannot be seen in these graphics. A full radial cycle of this orbit takes $T_r = 255.1M$, so the horizon is practically undistorted for a large fraction of this orbit. As the orbit oscillates above and below the equatorial plane, the horizon's bulge likewise oscillates above and below the plane. The bulge lags the orbit's ψ position, but leads[6] its θ position. This is basically the same behavior that we saw for the inclined circular Kerr orbit (Fig. 13) — Kerr-like in the axial direction, Schwarzschild-like in the polar direction. Having already examined the equatorial and the circular limits in detail, there are no surprises in Fig. 15. The interesting behaviors seen in the previously considered cases combine in the generic case in a very logical way.

VII. CONCLUSIONS

In this paper, we have taken the tools that we introduced in paper I for studying event horizons that are distorted by a strong-field (but small mass ratio) binary companion, and have applied them to eccentric and inclined binaries. For such orbits, the on-horizon tidal field varies significantly over the course of an orbit, leading to dynamical event horizon behavior. We have studied these horizon dynamics with multiple measures, examining the phase offset between the applied tide and the resulting shear to the horizons, as well as examining embeddings of the distorted horizons in a globally Euclidean 3-space.

Many of the results we have found follow in a fairly natural and logical way from results that were shown in paper I. In particular, we find that tidal bulges tend to lead the position of the orbiting body for very slow black

---

[5] This is why we show only a fraction of an orbit here. A full radial cycle of this orbit takes $T_r = 229.8M$, with the tide having a large impact only for $r \simeq r_{\rm min}$. The hole is practically undistorted for the majority of the orbit.

[6] The θ behavior of the bulge is only clear when the orbit is at periapsis. When the orbit is far from periapsis, the tidal deformation is gentle, and our algorithm for determining the position of the bulge becomes inaccurate due to discretization errors. The algorithm returns $\theta_{\rm bulge} = 90°$ in this case, corresponding to the largest radius of the undistorted Kerr embedding.
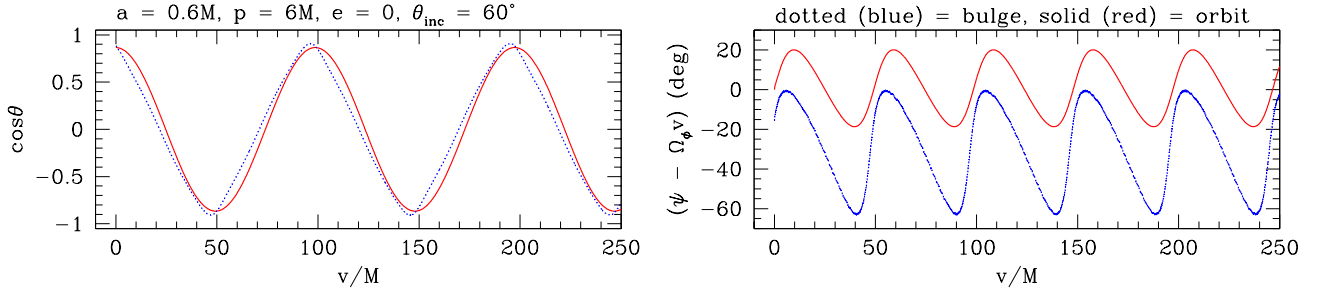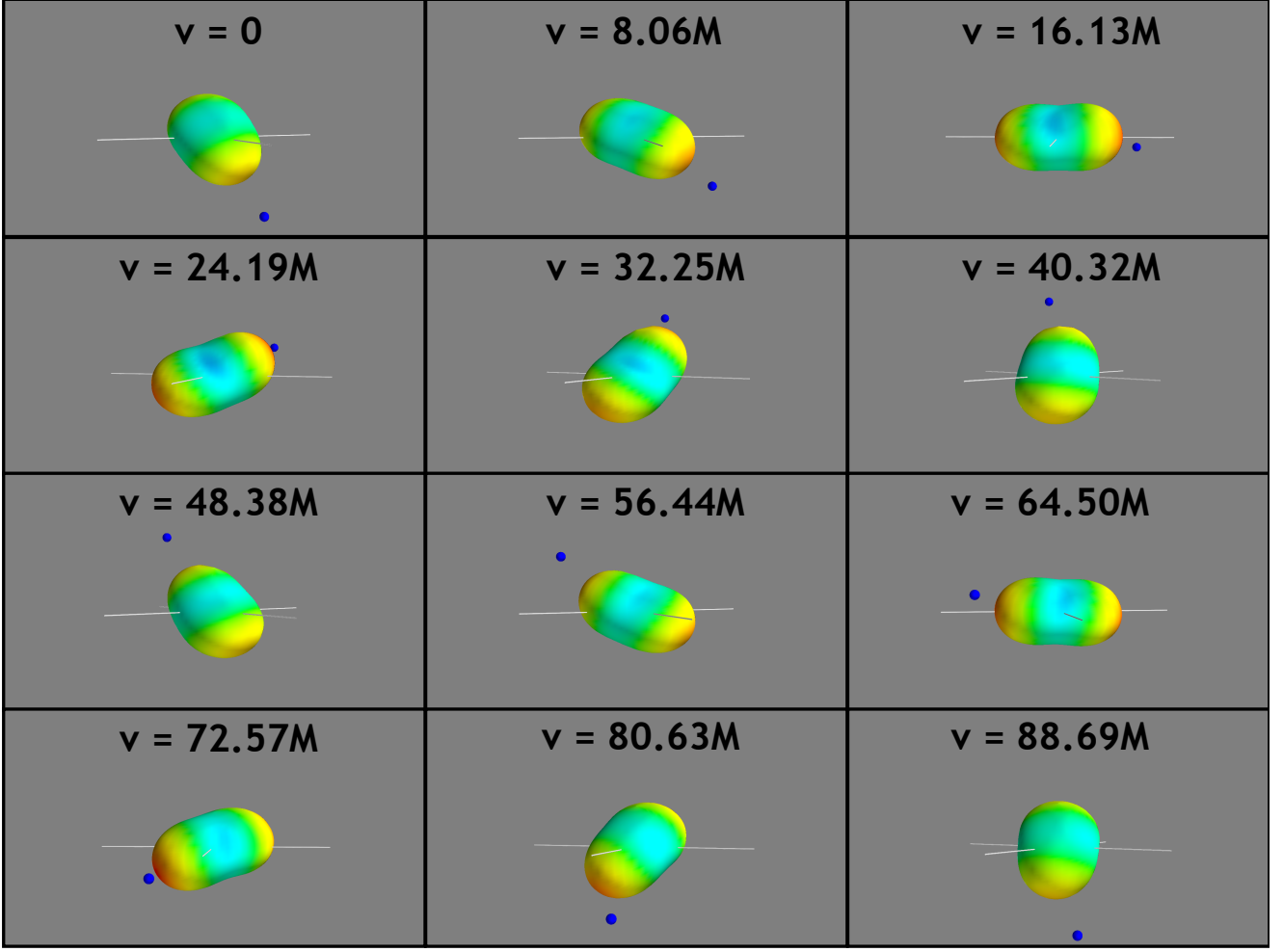
FIG. 13: Identical to Fig. 12, except that the black hole shown here is spinning with Kerr parameter $a = 0.6M$. As in Fig. 12, the axes indicate the hole's equatorial plane. In this plot, these axes rotate with the event horizon at frequency $\Omega_H = a/2Mr_+ = 1/6M$ (corresponding to a rotation period $T_H = 2\pi/\Omega_H = 37.7M$). In this sequence, the orbiting body (small sphere, dark blue in color) begins near the face close to the camera on the lower right-hand side of the black hole. It then sweeps up, crossing the equator soon after $v = 16.13M$, passes behind the black hole, and then descends downward again, crossing the equator soon after $v = 64.5M$. The horizon's distortions in this case do not move in lockstep with the orbiting body. Instead, the horizon exhibits mild shape variations. This is because the hole is not spherically symmetric, and so the tidal field acting on the horizon varies slightly over the orbit. Notice that the horizon's bulge leads the angular position of the orbit in the polar (θ) direction, but lags its position in the axial (ψ) direction; this can be seen in the snapshots, but is especially clear in the angle versus time plots shown in the bottom two panels. (We subtract $\Omega_\phi v$ from ψ to remove the uninteresting secular growth in this angle over a single orbit.) The polar behavior is much like what we see for Schwarzschild or very slow rotation; the axial behavior is about the same as the behavior we saw for equatorial circular orbits in paper I. The animation from which these stills are taken is available at [28].

hole spin, but lag the orbit for fast black hole spin. This is exactly the teleological tidal behavior that was seen with the simpler orbits we examined in paper I. We find an interesting variant of this behavior in the present analysis by looking at orbits that are inclined with respect to the hole's equatorial plane: the bulge tends to lead the orbit in the θ direction ("Schwarzschild-like" behavior), but lags the orbit for rapid spin in the ψ direction ("Kerr-like" behavior). The fact that the bulge exhibits different behavior with respect to the two angles is not surprising, since the hole rotates in the direction of ψ.

One interesting new behavior we have found are the low-amplitude, high-frequency wiggles which appear in the shear σ associated with the distortion of nearly extremal ($a \gtrsim 0.9995M$) black holes. A perhaps related low-amplitude, high-frequency wiggle is apparent in the horizon embedding of more slowly rotating ($a = 0.85M$) black holes. We have not succeeded in constructing a compelling explanation for these features. Although we can estimate the frequency of the wiggles fairly well, we cannot link them to other frequencies in the problem; and, the rate at which the oscillations decay with time does not appear to relate to other timescales in the problem, such as the correlation time κ^{-1} associated with the Green's function which connects to the tide to the shear. We hope that future work will elucidate the nature of this interesting phenomenon.

Acknowledgments

Appendix A: Newman-Penrose fields and on-horizon tensors

In this paper, we work with quantities that are based on Newman-Penrose fields such as the complex curvature scalar Ψ_0. Other papers, notably VPM11, use tensors which live in the manifold defined by the black hole's event horizon. There is a simple one-to-one correspondence between these two representations for the quantities which are important for our analysis. We develop this correspondence in this appendix.

We begin by defining some notation and background. As elsewhere in this paper, we use ingoing Kerr coordinates (v, r, θ, ψ) here. Components of tensors in the

2-dimensional manifold of the black hole's event horizon are labeled with upper-case Latin indices; these components range over the set (θ, ψ). (As elsewhere, Greek indices denote tensors in 4-dimensional spacetime.) Define the projection tensor $P^A{}_\alpha$, whose components in ingoing Kerr coordinates are given by the matrix

$$P^A{}_\alpha \doteq \begin{pmatrix} 0 & 0 & 1 & 0 \\ 0 & 0 & 0 & 1 \end{pmatrix} ; \qquad (A1)$$

the components of the inverse tensor $P^\beta{}_B$ are the transpose of this. When this operates on tensors at $r = r_+$, it projects quantities onto a slice of constant v on the horizon. At a given moment on the horizon, the spacetime's line element (2.1) becomes

$$ds^2 = g_{AB}dx^A dx^B = \Sigma_+ \, d\theta^2 + \frac{4M^2 r_+^2 \sin^2 \theta}{\Sigma_+} d\psi^2 , \ (A2)$$

where $\Sigma_+ = r_+^2 + a^2 \cos^2 \theta$. Finally, we will need the Newman-Penrose null legs in the Hawking-Hartle representation [10, 23]; these are given in Eqs. (2.8)–(2.10). For $r \to r_+$,

$$l^\mu \rightarrow [1, 0, 0, a\Omega_\mathrm{H}] , \qquad (A3)$$

$$m^\mu \rightarrow \frac{1}{\sqrt{2}(r_+ + ia \cos \theta)} [0, 0, 1, i(\csc \theta - a\Omega_\mathrm{H} \sin \theta)] . $$
$$(A4)$$

(We will not need n^μ.) At $r = r_+$, l^μ is tangent to the null generators of an unperturbed Kerr hole's horizon. Let us manipulate $m^\mu(r_+)$: we write

$$\begin{aligned} m^A(r_+) &\equiv m^\mu(r_+) P^A{}_\mu \\ &= \frac{1}{\sqrt{2}} \left(\alpha^A + i\beta^A \right) , \qquad (A5) \end{aligned}$$

where

$$\alpha^A \doteq \frac{1}{\Sigma_+} [r_+, a \cos \theta (\csc \theta - a\Omega_\mathrm{H} \sin \theta)] , \quad (A6)$$

$$\beta^A \doteq \frac{1}{\Sigma_+} [-a \cos \theta, r_+ (\csc \theta - a\Omega_\mathrm{H} \sin \theta)] . \ (A7)$$

Notice that $g_{AB}\alpha^A \alpha^B = 1$, $g_{AB}\beta^A \beta^B = 1$, $g_{AB}\alpha^A \beta^B = 0$.

The intrinsic geometry of the horizon is governed by the Weyl curvature. In our analysis, we use the Newman-Penrose scalar Ψ_0, which is given by

$$\Psi_0 = -C_{\mu\alpha\nu\beta} l^\mu m^\alpha l^\nu m^\beta . \qquad (A8)$$

Our focus is on this quantity on the horizon. Let us define

$$C_{AB} \equiv \left(C_{\mu\alpha\nu\beta} \, l^\mu P^\alpha{}_A \, l^\nu P^\beta{}_B \right)_{r_+} , \qquad (A9)$$

where the subscripted r_+ means that all the quantities in parentheses are to be evaluated at $r = r_+$. This definition
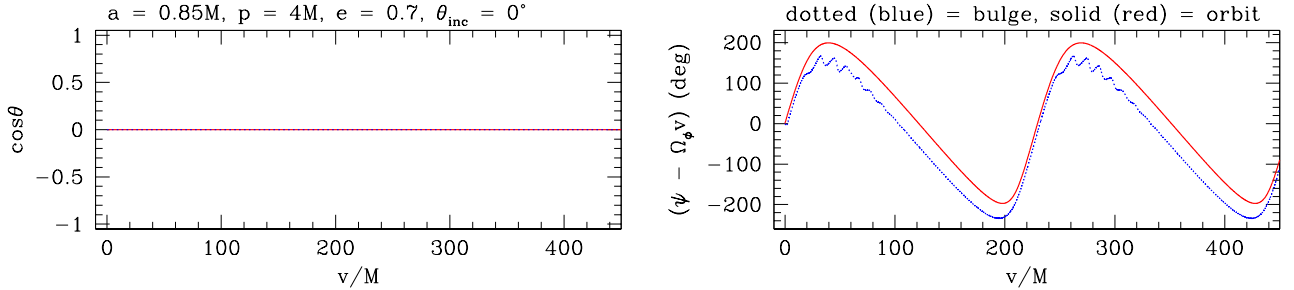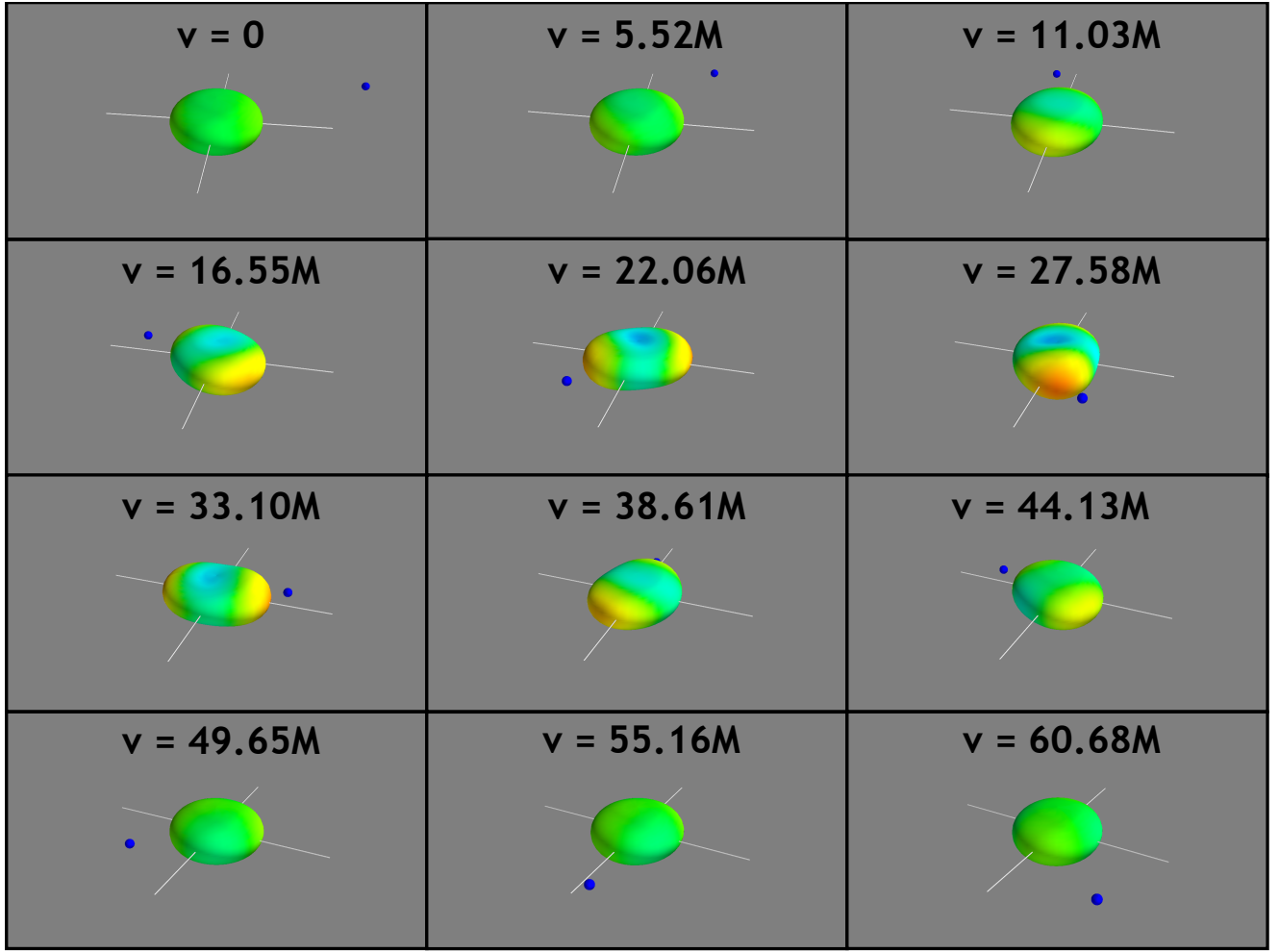
FIG. 14: Snapshots of an animation depicting an embedding of the distorted horizon for an equatorial eccentric orbit of a rapidly spinning Kerr black hole ($a = 0.85M$). The spin is nearly the largest value for which a Euclidean embedding of the undistorted horizon exists; the undistorted embedding geometry at this spin is of an axially symmetric oblate spheroid that is nearly flat at its poles. The orbit has semi-latus rectum $p = 4M$ and eccentricity $e = 0.7$, so its orbital radius varies from $r_{\max} = 13.33M$ to $r_{\min} = 2.34M$. As in Fig. 13, the axes indicating the equatorial plane rotate at the horizon frequency $\Omega_{\rm H} = a/2Mr_+$, corresponding to period $T_{\rm H} = 22.6M$. The axes complete a quarter turn every $5.6M$; this is very close to the cadence with which we sample this animation, so the axes appear nearly stationary in this sequence. The orbiting body is shown moving from roughly $r_{\max}/2$ to $r_{\min}$, and back out to roughly $r_{\max}/2$. For the first and last few stills shown here, the embedded horizon is nearly identical to that of an undistorted Kerr black hole. The embedded horizon by contrast is highly distorted in stills corresponding to $r \simeq r_{\min}$ ($16.55M \leq v \leq 44.13M$). This reflects the fact that the tidal field varies at leading order as $1/r^3$, which changes by a factor $(1 + e)^3/(1 - e)^3$ over an eccentric orbit. The tidal field thus varies by a factor ~ 180 for this orbit; even over this limited segment (for which the orbit only goes out to about $r_{\max}/2$), the tidal field varies by $\sim 180/8 \simeq 22$. The horizon bulge lags the particle's position in ψ at all times, consistent with the behavior seen and discussed in paper I for rapidly rotating Kerr black holes. (The θ behavior is uninteresting, since this is an equtorial orbit.) The high-frequency wiggles in the ψ-position of the bulge near $v \simeq 40M$ and $v \simeq 260M$ are perhaps related to the high-spin phenomenon discussed in Sec. V B. The animation from which these stills are taken is available at [28].

is identical to that in VPM11 [see text following their Eq. (2.30)]. Using this, on the horizon we have

$$
\begin{aligned}
\Psi_0 &= -C_{AB}m^A m^B \\
&= -\frac{1}{2}C_{AB}\left(\alpha^A\alpha^B - \beta^A\beta^B + i\alpha^A\beta^B + i\beta^A\alpha^B\right) \\
&\equiv -C_{AB}\left(e_+^{AB} + ie_\times^{AB}\right) .
\end{aligned}
\tag{A10}
$$

On the second line, we used Eq. (A5); on the third, we introduced the polarization tensors

$$
e_+^{AB} = \frac{1}{2}\left(\alpha^A\alpha^B - \beta^A\beta^B\right) , \tag{A11}
$$

$$
e_\times^{AB} = \frac{1}{2}\left(\alpha^A\beta^B + \beta^A\alpha^B\right) . \tag{A12}
$$

We further simplify Eq. (A10) by defining the Weyl polarization components:

$$
C_+ \equiv C_{AB}e_+^{AB} , \tag{A13}
$$

$$
C_\times \equiv C_{AB}e_\times^{AB} , \tag{A14}
$$

yielding

$$
\Psi_0 = -\left(C_+ + iC_\times\right) . \tag{A15}
$$

In other words, the on-horizon Weyl polarizations are simply the real and imaginary parts of Ψ_0 on the horizon, modulo an overall sign.

Lowering indices on the polarization tensors,

$$
e_{AB}^+ = g_{AC}g_{BD}e_+^{CD} , \tag{A16}
$$

$$
e_{AB}^\times = g_{AC}g_{BD}e_\times^{CD} , \tag{A17}
$$

allows us to construct the on-horizon Weyl tensor from the polarization components:

$$
C_{AB} = C_+ e_{AB}^+ + C_\times e_{AB}^\times . \tag{A18}
$$

Another important Newman-Penrose quantity which we can analyze in this manner is the spin coefficient

$$
\sigma = m^\mu m^\nu \nabla_\mu l_\nu . \tag{A19}
$$

At $r = r_+$, this describes the shear of the horizon's generators. Because $m^v = m^r = 0$ at $r = r_+$, we have

$$
\sigma(r_+) = \left(m^A m^B \nabla_A l_B\right)_{r_+} . \tag{A20}
$$

Define

$$
\sigma_{AB} = \frac{1}{2}\left(\nabla_A l_B + \nabla_B l_A\right)_{r_+} . \tag{A21}
$$

Note that σ_{AB} is trace free since $\nabla_A l^A = 0$ on the horizon. This definition of the shear tensor for the horizon's null generators is therefore equivalent to that used in VPM11 [compare their Eqs. (2.11) and (2.15)]. Using Eqs. (A5), (A16), and (A17), we find

$$
\begin{aligned}
\sigma(r_+) &= \sigma_{AB}\left(e_+^{AB} + ie_\times^{AB}\right) \\
&= \sigma_+ + i\sigma_\times .
\end{aligned}
\tag{A22}
$$

The shear polarizations written here were introduced by VPM11; they are defined in a manner analogous to C_+ and $C_\times$, and are just the real and the imaginary parts of the Newman-Penrose quantity σ.
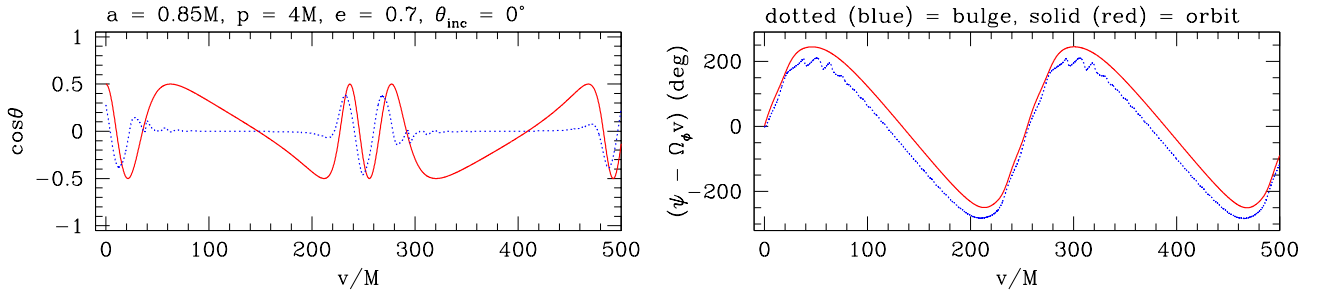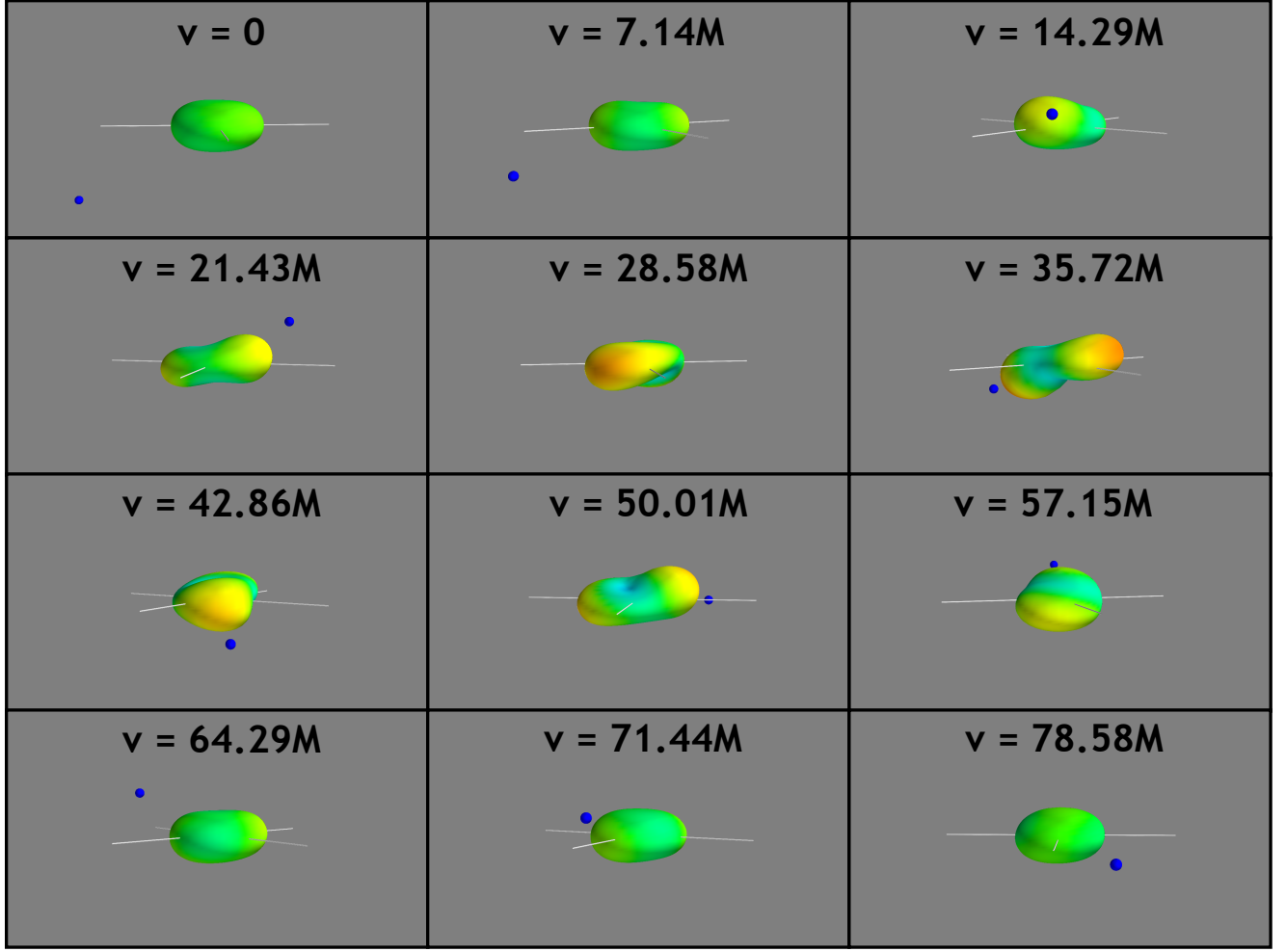
FIG. 15: Snapshots of an animation depicting an embedding of the distorted horizon for a generic orbit of a rapidly spinning Kerr black hole ($a = 0.85M$). The system is nearly identical to that used in Fig. 14, but we have inclined the orbit to $\theta_{\text{inc}} = 30°$. The orbiting body is again shown moving from roughly $r_{\text{max}}/2$ to r_{min}, and back out to roughly $r_{\text{max}}/2$. The horizon's dynamics here shares features with both the equatorial case depicted in Fig. 14 and the inclined cases in Figs. 12 and 13. In particular, the horizon varies from nearly undistorted when $r \simeq r_{\text{max}}/2$ (roughly first and last stills in this sequence) to highly distorted when $r \simeq r_{\text{min}}$ (stills from $28.52M \leq v \leq 57.15M$), in a manner qualitatively similar to the eccentric equatorial case. However, the horizon bulge flexes above and below the plane as the orbital motion oscillates in the polar direction, very much like the circular inclined cases. The panels illustrating $\cos\theta$ and ψ versus time shows that the bulge lags the body in ψ. At periapsis, the bulge lags the body the body in θ. This is exactly the same offset behavior that was seen in the circular inclined Kerr case shown in Fig. 13. (When the orbiting body is far from periapsis, the location of the bulge is difficult to determine accurately; our code returns $\theta = 90°$ for the bulge's position, reflecting the oblate spheroid shape of the undistorted black hole.) The animation from which these stills are taken is available at [28].

[1] J. S. Read, C. Markakis, M. Shibata, K. Uryu, J. D. E. Creighton, and J. L. Friedman, Phys. Rev. D **79**, 124033 (2009).

[2] T. Hinderer, B. D. Lackey, R. N. Lang, and J. S. Read, Phys. Rev. D **81**, 123016 (2010).

[3] T. Damour, A. Nagar, and L. Villain, Phys. Rev. D **85**, 123007 (2012).

[4] T. Damour and A. Nagar, Phys. Rev. D **80**, 084035 (2009).

[5] T. Binnington and E. Poisson, Phys. Rev. D **80**, 084018 (2009).

[6] L. Baiotti, T. Damour, B. Giacomazzo, A. Nagar, and L. Rezzolla, Phys. Rev. Lett. **105**, 261101 (2010).

[7] N. N. Weinberg, P. Arras, and J. Burkart, Astrophys. J. **769**, 121 (2013).

[8] T. Venumadhav, A. Zimmerman, and C. M. Hirata, Astrophys. J. **781**, 23 (2014).

[9] S. A. Teukolsky, Astrophys. J. **185**, 635 (1973).

[10] S. A. Teukolsky and W. H. Press, Astrophys. J. **193**, 443 (1974).

[11] S. A. Hughes, Phys. Rev. D **61**, 084004 (2000).

[12] S. A. Hughes, Phys. Rev. D **64**, 064004 (2001).

[13] T. Damour and O. M. Lecian, Phys. Rev. D **80**, 044017 (2009).

[14] S. Taylor and E. Poisson, Phys. Rev. D **78**, 084016 (2008).

[15] E. Poisson and I. Vlasov, Phys. Rev. D **81**, 024029 (2010).

[16] I. Vega, E. Poisson, and R. Massey, Class. Quantum Grav. **28**, 175006 (2011).

[17] H. Fang and G. Lovelace, Phys. Rev. D **72**, 124016 (2005).

[18] E. Poisson, Phys. Rev. D **91**, 044004 (2015).

[19] P. Pani, L. Gualtieri, A. Maselli, and V. Ferrari, arXiv:1503.07365.

[20] S. O'Sullivan and S. A. Hughes, Phys. Rev. D, in press.

[21] S. Drasco and S. A. Hughes, Phys. Rev. D **73**, 024027 (2006).

[22] L. Smarr, Phys. Rev. D **7**, 289 (1973).

[23] S. W. Hawking and J. B. Hartle, Commun. Math. Phys. **27**, 283 (1972).

[24] J. B. Hartle, Phys. Rev. D **8**, 1010 (1973).

[25] J. B. Hartle, Phys. Rev. D **9**, 2749 (1974).

[26] K. S. Thorne, R. H. Price, and D. A. MacDonald, *Black Holes: The Membrane Paradigm* (Yale University Press, New Haven, 1986).

[27] V. Cardoso and P. Pani, Class. Quantum Grav. **30**, 045011 (2013).

[28] http://gmunu.mit.edu/viz/embed_viz/embed_viz.html

[29] W. Schmidt, Class. Quantum Grav. **19**, 2743 (2002).

[30] R. Fujita and W. Hikida, Class. Quantum Grav. **26**, 135002 (2009).

[31] A. A. Starobinski and S. M. Churilov, Zh. Eksp. Teor. Fiz. **65**, 3 (1973) [Sov. Phys. JETP **38**, 1 (1974)].

[32] G. W. Gibbons, C. A. R. Hardeiro, and C. Rebelo, Phys. Rev. D **80**, 044014 (2009).

[33] K. Glampedakis and D. Kennefick, Phys. Rev. D **66**, 044002 (2002).

[34] W. Throwe and S. A. Hughes, in preparation; preliminary version available as W. Throwe, unpublished MIT undergraduate thesis (2010).

[35] F. D. Ryan, Phys. Rev. D **53**, 3064 (1996).

[36] D. Kennefick and A. Ori, Phys. Rev. D **53**, 3064 (1996).

[37] Y. Mino, unpublished Ph. D. thesis, Kyoto University, 1996.

[38] E. E. Flanagan and T. Hinderer, in preparation.